The Astrophysical Journal, 1005:40 (24pp), 2026 July 1 https://doi.org/10.3847/1538-4357/ae7107

A Compton Reverberation Model for the Production of X-Ray Time Lags from Coupled Bursts in Black Hole Accretion Disks

Thunyapong Mahapol, Peter A. Becker, and Mario Gliozzi
Department of Physics & Astronomy, George Mason University, Fairfax, VA 22030-4444, USA; thunmm@gmail.com, pbecker@gmu.edu, mgliozzi@gmu.edu
Received 2025 August 14; revised 2026 May 1; accepted 2026 May 19; published 2026 June 23

Abstract

X-ray Fourier time lags detected from accreting black holes in active galactic nuclei (AGNs) provide important glimpses into the high-energy processes occurring near the event horizon. For many narrow-line Seyfert 1 (NLS1) galaxies, the lag–frequency distribution displays multiple sign changes, indicating several transitions between hard and soft time lags. We develop a new Compton reverberation model that can reproduce the observed time lag distributions for multiple NLS1 galaxies, based on the Compton reprocessing of iron K and L seed photons that are injected in two coupled bursts occurring at different radii in the disk. The variability is driven by transient high-energy emission generated by the Compton upscattering in the hot corona of soft thermal photons produced in the cool outer region of the accretion disk. The two bursts of K and L seed photons are linked by a pressure wave that propagates outward and deposits its energy near the standing shock at the outer boundary of the hot inner region, triggering the second burst. The new model is based on a Fourier-transformed, vertically averaged radiation transport equation. We use our new model to analyze and interpret the observational time lag data for the NLS1 galaxies 1H 0707−495, Ark 564, NGC 4051, and Mrk 766. We demonstrate that the incorporation of a second seed photon burst allows our model to accurately reproduce the time lag data for several AGNs that display complex time lag patterns, including multiple sign changes. We also discuss the physical scenario for connecting the two coupled bursts.

Unified Astronomy Thesaurus concepts: Active galactic nuclei (16); Galaxy accretion disks (562); High energy astrophysics (739); Supermassive black holes (1663); X-ray astronomy (1810); Theoretical models (2107)

1. Introduction

Fourier time lags are commonly observed in systems in which matter is accreting onto a compact object such as a black hole or a neutron star. These time lags are derived from phase lags between Fourier-transformed light curves in hard (high-energy) and soft (low-energy) X-ray bands (W. Alston et al. 2020). In the case of active galactic nuclei (AGNs), which are sources of highly variable X-ray emission, Fourier time lags are thought to originate from X-rays emitted by the infalling hot plasma around the central supermassive black hole that experience Compton scattering as they diffuse through the plasma. Depending on the timescale, the variability in the X-ray light curves at different energy channels may lead or lag one another. Typically, one finds that at long timescales, the variability of hard X-rays tends to lag that of soft X-rays, which is called a "hard lag." The opposite scenario is called a "soft lag."

1.1. NLS1 Time Lag Observations

Hard lags have been commonly detected in AGNs over the past four decades (e.g., G. Hasinger et al. 1986; M. van der Klis et al. 1987; Y. E. Lyubarskii 1997; P. Arévalo & P. Uttley 2006). More recently, A. C. Fabian et al. (2009) have analyzed sources that display more complex structures, in which the time lags may be either hard or soft, depending on the Fourier frequency (e.g., B. De Marco et al. 2013; E. Kara et al. 2013b; J. J. Kroon & P. A. Becker 2016; D. C. Baughman & P. A. Becker 2022). Examples include 1H 0707−495, Ark 564, NGC 4051, and Mrk 766. There are two distinct scenarios for the production of X-ray time lags in AGNs, depending on whether one is focusing on hard or soft lags. Most of the early studies suggested that the emergence of hard lags is a natural consequence of the time required to Compton-upscatter soft seed photons by hot electrons (M. van der Klis et al. 1987; S. Miyamoto et al. 1988). The explanation for the production of the observed soft lags is less clear, and several alternative scenarios have been proposed.

The idea of using Fourier transformation to analyze time lags between two light curves at different energies as a function of Fourier frequency, $\nu_{\rm F}$, or the inverse of the corresponding observed variability timescale, was first introduced by M. van der Klis et al. (1987) and further developed by M. A. Nowak et al. (1999). For the case of radio-quiet AGNs, the observed X-ray time lag δt is comparable to the light-crossing time for one gravitational radius, $R_g/c \equiv GM/c^3 \approx 50\,{\rm s}\,(M/10^7 M_\odot)$ where M is the mass of the central black hole, as it falls in the range $\delta t \sim 10-100\,{\rm s}$ for Fourier frequencies of $10^{-4}\,{\rm Hz} \lesssim \nu_{\rm F} \lesssim 10^{-3}\,{\rm Hz}$ (e.g., B. De Marco et al. 2013). This suggests that the physical processes occurring in the inner region of the accretion disk can be probed via analysis of the observed Fourier time lag distribution.

1.2. Theoretical Challenges

The occurrence of both hard and soft X-ray time lags in the same set of observations for some narrow-line Seyfert type 1 (NLS1) galaxies presents serious challenges for theoretical models attempting to simulate the observed X-ray variability. The complex variation of the Fourier time lags as a function of the Fourier frequency for NLS1 sources has proven difficult to explain using simple one-zone models. This has led to a proliferation of theoretical ideas that focus on the reverberation and reprocessing of hard X-ray photons in a cool region of the disk to explain the soft lags, combined with the Compton upscattering of soft X-rays in a high-temperature corona to account for the hard lags. The various models were discussed by A. C. Fabian et al. (2012) and we briefly review some of these ideas here.

One of the earliest explanations for the soft lags observed in some sources was proposed by J. Malzac & E. Jourdain (2000), who suggested that hard X-ray photons are reprocessed in a cooling region, in which the temperature of the scattering electron decreases on a timescale similar to the soft lag time. They suggested a picture in which the soft lags are a manifestation of the reprocessing of flare emission originating in the corona. The flare initially heats the disk plasma, and subsequently the disk reprocesses the X-ray photons as it cools. The model proposed by these authors is generic, and they did not attempt to fit the data for any source. It was subsequently pointed out by A. Zoghbi et al. (2010) that the model of J. Malzac & E. Jourdain (2000) cannot explain an abrupt change in the observed variability pattern in the spectrum of 1H 0707−495 above and below 1 keV.

An alternative physical picture was suggested by A. C. Fabian et al. (2009) and A. Zoghbi et al. (2010), who argued that the soft lags detected from 1H 0707−495 reflect the time required by hard X-ray photons created in a hot inner corona that downscatter off cooler material in the underlying disk. In this so-called "lamppost" model, high-energy emission generated via the upscattering in a hot central corona of soft thermal photons generated in the cool outer disk leads to illumination of the underlying inner region of the disk, resulting in the "reverberation" of these photons toward the observer. This model relies on a rather complex geometrical picture, and the fits to the observed X-ray spectra often involve multiple power-law components, a blackbody component, and multiple reflection components (E. Kara et al. 2013a). Some applications also invoke scattering and absorption in a putative wind (T. Dauser et al. 2012; M. Mizumoto et al. 2019; M. Szanecki et al. 2020; T. Boller et al. 2021). Despite its complexity, the reverberation scenario has proven successful due to its ability to fit the observed spectral data for multiple NLS1 sources. For example, A. Zoghbi et al. (2010) utilized this scenario to interpret the soft lags from 1H 0707−495, although L. Miller et al. (2010a) suggested that the relative time lags between three X-ray bands observed in 1H 0707 −495 are inconsistent with this model, and that a more extended scattering region is required. Moreover, E. Gardner & C. Done (2014) observed PG 1244+026, an NLS1 galaxy, and found that pure reflection is insufficient to cause the soft lags, implying that the radiation experiences additional reprocessing in the accretion disk.

D. C. Baughman & P. A. Becker (2022) developed a spherically symmetric accretion model that successfully explains the occurrence of both hard and soft lags in 1H 0707−495. This model uses the $\rho \propto r^{-3/2}$ density distribution proposed by X.-M. Hua et al. (1997, 1999) in their model for the time lags generated in Cyg X-1. This model suggests that the observed time lags are the combined effect of bulk and thermal Comptonization operating in a quasi-spherical corona that is free-falling onto the central black hole. Their model utilizes the closed-form solution to a radiation transport equation that includes the effect of Comptonization to explain the reprocessing of an iron L-line seed photon flash emitted from a spherical shell source. While they successfully reproduced the Fourier lag–frequency distribution for 1H 0707−495, they did not account for the rotational motion or the shear of the accreting gas, nor did they treat the possibility of iron K photon injection.

1.3. Steady-state X-Ray Spectra

The steady-state (time-averaged) X-ray continuum spectrum observed from a typical NLS1 galaxy exhibits a soft blackbody excess in the ∼0.1−1 keV energy range and a steep power-law region component extending from ∼1 to 10 keV that is apparently heavily modified by a complex absorption process that may also involve reflection from the inner disk (T. Boller et al. 1996; S. Komossa 2008). In this scenario, a hard spectrum emitted from a hot, central "lamppost" X-ray corona illuminates the inner disk and is reprocessed by thermal matter before being reemitted (A. C. Fabian et al. 2002; L. C. Gallo 2006). NLS1 spectra also exhibit a sharp decline in the 5–10 keV energy range, for which a variety of explanations have been proposed, depending on the source. For example, in the cases of 1H 0707−495 and Ark 564, the decline in the spectrum in the ∼5−10 keV energy range has been interpreted as either an absorption line or the low-energy wing of an iron emission line (I. E. Papadakis et al. 2007; A. C. Fabian et al. 2012). On the other hand, in the case of NGC 4051, this feature has been attributed to a combination of an iron emission line and a recombination edge component (E. Seifina et al. 2018). Finally, in the case of Mrk 766, the sharp decline observed in the 7–10 keV energy range is thought to be related to emission and absorption, combined with unsaturated thermal Comptonization in a relatively low-temperature gas (S. Giacchè et al. 2014). These processes may operate in addition to thermal bremsstrahlung, which characteristically produces a relatively soft X-ray emission component in NLS1 galaxies. Furthermore, the observed spectra may also be affected by other processes, such as reddening and relativistic blurring (e.g., A. C. Fabian et al. 2012). The diversity of radiation mechanisms thought to be involved in the formation of the steady-state X-ray spectra in NLS1 galaxies makes it challenging to connect this process with the production of the time-variable emission that we focus on here, which may result from a completely different physical mechanism.

The X-ray spectrum from the corona is the result of the upscattering of soft UV photons emitted from the outer cool region of the disk (F. Haardt & L. Maraschi 1991, 1993; D. R. Wilkins et al. 2016, 2022). The primary spectrum from the corona is a Comptonized power law with photon spectral index $\Gamma \sim 2$, resulting from the combination of a high electron temperature, $T_e \sim 10^9$ K, and a moderate electron scattering optical depth, $\tau \sim 1$ (M. Mizumoto et al. 2019; M. Szanecki et al. 2020; T. Boller et al. 2021). For a steady-state situation in which $\dot{N}_{\rm UV}$ photons with energy $\dot{E}_{\rm UV}$ are injected per unit time into the corona, it is straightforward to show that the resulting X-ray photon number spectrum emitted from the corona for the case of unsaturated Comptonization is given by (G. B. Rybicki & A. P. Lightman 1979; R. A. Sunyaev & L. G. Titarchuk 1980)

$$N_{\rm X} = (\Gamma - 1)\,\frac{\dot{N}_{\rm UV}}{E_{\rm UV}}\left(\frac{E}{E_{\rm UV}}\right)^{-\Gamma}, \tag{1}$$

where the index Γ is computed using

$$\Gamma = -\frac{1}{2} + \sqrt{\frac{9}{4} + \frac{4}{y}}, \tag{2}$$

and y denotes the Compton y-parameter, which is related to T_e and τ via

$$y = \frac{4kT_e}{m_e c^2}\,\mathrm{Max}(\tau,\,\tau^2). \tag{3}$$

The full energy range of the hard X-ray spectrum from the corona is not detected in the spectra observed from NSL1 galaxies, which tend to be quite soft. However, a portion of the direct emission from the corona may be visible (L. Miller et al. 2010a, 2010b). In the standard reflection scenario, Equation (1) represents the hard X-ray spectrum emitted from the hot corona that illuminates the underlying disk and is reprocessed by thermal matter before being reemitted (M. Mizumoto et al. 2019; M. Szanecki et al. 2020; T. Boller et al. 2021).

1.4. This Paper

In previous work (T. Mahapol & P. A. Becker 2024, hereafter Paper I), we developed a detailed, rigorous model for time lags emanating from AGN accretion disks in which fluorescent iron K and L photons experience Compton reverberation in the accreting plasma before escaping to form the time-dependent part of the observed X-ray spectrum. The model discussed in Paper I successfully reproduces the Fourier time lag–frequency distributions for the two NLS1 galaxies 1H 0707−495 and Ark 564. These two sources display relatively simple time lag distributions, in which there is only one sign change, indicating only one transition between the hard and soft lags. However, many other sources, such as Mrk 766 and NGC 4051, display multiple sign changes, indicating multiple transitions between soft and hard lags occurring at different Fourier frequencies. In order to explain the complex behavior of these sources, we argue that a generalized model is required, in which the seed photons are injected in two separate bursts that occur at different radii in the disk, and at different times, and involve photons injected with two different energies.

In this paper, we develop a new coupled-burst Compton reverberation model for simulating the complex time lag distributions observed in NLS1 sources that display multiple changes in the sign of the time lag. In the context of our model, Compton reverberation refers to the effect of thermal and bulk Comptonization, combined with the diffusive and advective transport of seed photons injected into the hot inner region of the accretion disk. We show that the new model can reproduce the observed time lag distributions for multiple NLS1 galaxies, based on the Compton reprocessing of iron K and L seed photons that are injected in two coupled bursts occurring at different radii in the disk. In the scenario envisioned here, the fundamental mechanism driving the variability characterized by the time lags is the transient acceleration of hot electrons in the corona via magnetic reconnection (J. Malzac & E. Jourdain 2000; A. Zoghbi et al. 2010).

The formation of the X-ray time lags begins with an impulsive reconnection event in the corona that heats the electrons to temperature $T_e \sim 10^9$ K (P. Uttley et al. 2014; K. Fukumura et al. 2016; D. R. Wilkins et al. 2022). The accelerated electrons generate X-rays via the upscattering of soft thermal UV photons produced in the cool outer region of the accretion disk. The resulting Compton cooling lowers the electron temperature to $T_e \sim 5 \times 10^8$ K at the end of the event (D. R. Wilkins et al. 2022). The hot central corona is located within a few gravitational radii of the black hole, and therefore the emitted X-rays are subject to strong gravitational deflection (light bending), which directs a large fraction of the X-ray flash downward from the corona onto the hot inner region of the disk (A. C. Fabian & S. Vaughan 2003; G. Miniutti & A. C. Fabian 2004; A. Zoghbi et al. 2010). The illumination of the disk causes the excitation of iron atoms, which leads to the production of fluorescent iron K and L photons with energies $\epsilon_{\rm K}$ and $\epsilon_{\rm L}$, respectively, at radius r_1 and time t_1 (A. C. Fabian et al. 2012; M. Mizumoto et al. 2018; T. Boller et al. 2021). These photons are subsequently reprocessed in the disk, before escaping to contribute to the observed X-ray spectrum. The illumination of the inner region of the disk also triggers a thermal instability, and the energy from this instability drives a pressure wave that transports energy outward at the speed of sound. This energy is ultimately dissipated in the vicinity of the standing shock wave located at the outer boundary of the hot inner region, because the pressure wave cannot propagate upstream into the supersonic region beyond the standing shock. The dissipated energy produces a flash of bremsstrahlung radiation, which generates another group of iron K and L seed photons at radius r_2 and time t_2, as a result of iron fluorescence. The production of fluorescent iron K and L photons in our model and their subsequent reprocessing via Compton scattering and advection is a variation of the standard reflection scenario that focuses on the detailed time-dependent radiative transfer occurring in the accretion disk.

The theoretical formalism is based on a Fourier-transformed, vertically averaged radiation transport equation written in cylindrical coordinates. The transport equation governs the propagation of the K and L seed photons generated in the two coupled bursts. These photons subsequently get reprocessed before escaping from the disk. Because the transport equation is linear, we can treat the overall Fourier transform of the variable emission as the sum of the individual Fourier transforms for the two separate bursts. We demonstrate that the coupled-burst model is able to explain the complex Fourier time lag distributions observed from sources such as Mrk 766 and NGC 4051.

The paper is organized as follows. In Section 2, we summarize and formulate the fundamental equations for the coupled-burst model, including the Fourier-transformed radiation transport equation. In Section 3, we discuss the analytical solution to the Fourier-transformed transport equation, which is used to calculate X-ray time lags for the selected AGN sources. In Section 4, we apply the new model in order to interpret the X-ray time lag data for several sources displaying complex time lag behaviors, including 1H 0707−495, Ark 564, NGC 4051, and Mrk 766. In Section 5, we discuss the implications of our theoretical model and its relation to previously published work.

2. Model Overview

We formulate our theoretical model by suggesting that the detected hard and soft X-ray time lags in AGNs occur due to reverberations in both physical space and energy space, mediated by Compton scattering. The model is based on a cylindrical-symmetric radiation transport equation, developed

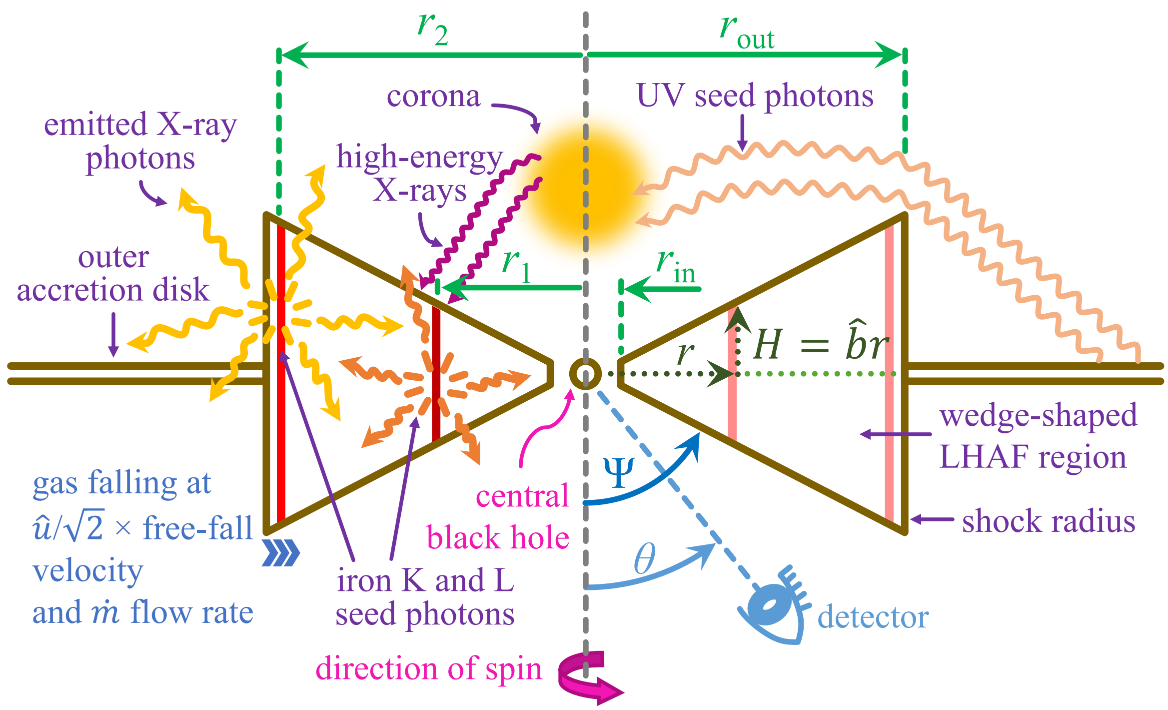

Figure 1. Schematic diagram of the structure of our modeled accretion disk. Our computational domain is the wedge-shaped, self-similar inner region with slope $\hat{b}$ surrounded by a geometrically thin, optically thick outer disk region. The hot inner region spans from the radius $r = r_{\rm in} = r_{\rm ISCO}$ to $r = r_{\rm out}$ which also coincides with the shock radius. The fluorescent iron K and L seed photons with energies $\epsilon_{\rm K}$ and $\epsilon_{\rm L}$, respectively, are injected in two bursts. The first occurs at radius r_1 and time t_1, and the second occurs at radius r_2 and time t_2. The inclination angle of the accretion disk is θ.

in Paper I and originally proposed by M. Colpi (1988), which describes the time-dependent vertically averaged X-ray spectrum inside the accretion disk. The solution to the equation can be used to find the spectrum of the "face" (the upper and lower surfaces) and "side" (the sidewall) of an accretion disk which is divided into a hot inner region and a cool outer region. Our objective here is to perform a detailed analysis of the radiation transport in the hot inner region where most high-energy photons are radiated.

To compute X-ray time lags, the Fourier-transformed X-ray light curves detected in different energy bands must be obtained. We therefore formulate our theoretical model in the Fourier domain. This can be done by writing a time-dependent radiation transport equation and applying Fourier transformation to the equation. The Fourier transform of the transport equation is then separated into an energy-dependent equation and a spatial-dependent equation. To solve these two decoupled equations, we ensure the spatial separation equation satisfies the free-streaming boundary conditions and solve for eigenvalues for the separation constant. We then combine the solutions to the spatial and energy separation equations to obtain the general solution for the Fourier-transformed emission spectrum inside the disk as a series expansion.

2.1. Coupled-burst Model

Similar to our single-burst model (Paper I), here we treat the hot inner region combined with the corona as a wedge-shaped, hot, tenuous accretion flow, which extends from the inner radius $r_{\rm in}$, coinciding with the innermost stable circular orbit, $r_{\rm ISCO}$, of the central black hole to the outer radius $r_{\rm out}$, which is the radius where the standing shock wave forms due to a local balance between centripetal, gravitational, and pressure gradient forces (e.g., S. Chakrabarti & L. G. Titarchuk 1995; S. K. Chakrabarti 1997a, 1997b). Thermodynamically, the standing shock regulates the transition between the cool, dense outer region of the accretion disk and the hot, tenuous inner region. For a black hole with mass M and angular momentum J, the value of $r_{\rm ISCO}$ is computed using (J. M. Bardeen et al. 1972)

$$
\begin{aligned}
r_{\rm ISCO} &= R_g\left[3 + Z_2 \mp (3 - Z_1)^{1/2}(3 + Z_1 + 2Z_2)^{1/2}\right],\\
Z_1 &\equiv 1 + (1 - a^2)^{1/3}[(1 + a)^{1/3} + (1 - a)^{1/3}],\\
Z_2 &\equiv \left(3a^2 + Z_1^2\right)^{1/2},
\end{aligned}
\tag{4}
$$

where $a = J/(McR_g)$ is the dimensionless spin parameter of the central black hole and the upper and lower signs refer to prograde and retrograde orbits, respectively. The hot inner region of the disk may have the form of an advection-dominated accretion flow (ADAF), if the accretion rate is sub-Eddington (see R. Narayan & I. Yi 1995), or in situations involving super-Eddington accretion, it may have the form of a luminous hot accretion flow (LHAF; see F. Yuan 2001).

As in our previous single-burst model (Paper I), we require that the radiation field satisfies free-streaming boundary conditions at the inner and outer radii. The radial accretion velocity profile, v_r, is assumed to be a fraction of the freefall velocity, $v_r \propto r^{-1/2}$, which agrees with the self-similar disk structure obtained by R. D. Blandford & M. C. Begelman (1999) in their study of ADAF disks. It is likely that a similar dynamical profile also describes accretion disks with an LHAF structure (see Section 2.3). The hot inner ADAF wedge is encompassed by a geometrically thin, optically thick outer disk (see Figure 1). We review the main features of the theoretical model below.

2.2. Fundamental Dynamical Relations

The X-ray emission observed in AGNs is powered fundamentally by the accretion of gas onto a central supermassive black hole. It is important to perform an analysis of the energy budget in order to develop a constraint on the value of the X-ray luminosity, L_X, for a given accretion rate, $\dot{M}$. Assuming that the kinetic energy is converted into radiation energy with efficiency $\eta_{\rm bol}$, the total radiation power, or bolometric luminosity, is

$$L_{\rm bol} = \eta_{\rm bol}\, \dot{M} c^2, \tag{5}$$

where $\eta_{\rm bol}$ is the bolometric efficiency, which is estimated to be in the range $\eta_{\rm bol} \sim 0.1{-}0.5$. This implies that most of the accretion power is absorbed by the black hole's event horizon. The accretion rate in the disk, $\dot{M}$, is given by

$$\dot{M} = 4\pi |\upsilon_r| r H \rho, \tag{6}$$

where ρ is the mass density, H is the half-thickness of the disk, r is the radius, and $\upsilon_r < 0$ is the radial velocity of the disk. For disks in hydrostatic equilibrium, the half-thickness is given by

$$H \approx \frac{a}{\Omega_K}, \tag{7}$$

where a is the adiabatic sound speed in the gas and $\Omega_K = (GM/r^3)^{1/2}$ is the Keplerian angular velocity. The Eddington luminosity, L_E, is the maximum radiation power that can be emitted before radiation pressure overwhelms the gravitational force. This quantity depends on the geometry of the radiating system, but assuming spherically symmetric accretion and emission, the Eddington luminosity is given by

$$L_E = \frac{4\pi G M c m_p}{\sigma_T} = \frac{4\pi c^3 R_g m_p}{\sigma_T}, \tag{8}$$

where σ_T is the Thomson cross section, m_p is the proton mass, and R_g is the gravitational radius, defined by

$$R_g = \frac{GM}{c^2}. \tag{9}$$

The associated Eddington accretion rate, $\dot{M}_E$, is given by

$$\dot{M}_E = \frac{1}{\eta_{\rm bol}} \frac{L_E}{c^2}, \tag{10}$$

or, equivalently,

$$\dot{M}_E = \frac{4\pi G M m_p}{\eta_{\rm bol}\, c\, \sigma_T} = \frac{4\pi c R_g m_p}{\eta_{\rm bol}\, \sigma_T}. \tag{11}$$

We can parameterize the accretion rate relative to the Eddington rate by introducing the dimensionless accretion rate, $\dot{m}$, defined by

$$\dot{m} \equiv \frac{\dot{M}}{\dot{M}_E} = \frac{L_{\rm bol}}{L_E}. \tag{12}$$

The value of $\dot{m}$ varies if the source contains a strong outflow or jet, which may occur in the outer regions of accretion disks in NLS1 galaxies. However, these outflows appear to occur at a radius $r_{\rm jet} \sim 1$ pc, which is a much larger scale than the radius of the hot inner region which is the region of interest here (B. Meena et al. 2021; Y. Xu et al. 2021). Hence, we will treat $\dot{m}$ as a constant throughout the remainder of this paper. The bolometric luminosity $L_{\rm bol}$ is related to the X-ray luminosity L_X via the bolometric correction, $\kappa_{\rm bol}$, defined by

$$\kappa_{\rm bol} \equiv \frac{L_{\rm bol}}{L_X}, \tag{13}$$

which is approximated to be $\kappa_{\rm bol} \sim 2$ in Paper I. We note that the definition of $\dot{m}$ we are using here is slightly different from the definition utilized in Paper I because we now include the bolometric efficiency, $\eta_{\rm bol}$, in the definition of $\dot{m}$ in accordance with the standard approach adopted in the literature. Hence, it follows that

$$\dot{m} = \eta_{\rm bol}\, \dot{m}_{\rm SB}, \tag{14}$$

where $\dot{m}_{\rm SB}$ denotes the definition of the dimensionless accretion rate used in the single-burst model discussed in Paper I. The corresponding expression for the X-ray luminosity is written as

$$\frac{L_X}{L_E} = \frac{1}{\kappa_{\rm bol}} \dot{m} = \frac{\eta_X}{\eta_{\rm bol}} \dot{m}, \tag{15}$$

where the X-ray efficiency, η_X, is defined by

$$\eta_X \equiv \frac{\eta_{\rm bol}}{\kappa_{\rm bol}}. \tag{16}$$

We note that η_X may have a different value from $\eta_{\rm bol}$ due to variations in the amount of radiation energy emitted in the outer, cooler UV/optical region of the accretion disk versus the hotter, optically thin X-ray emitting inner region.

2.3. Dynamical Structure of the Disk

Following the same procedure in Paper I, we define the dimensionless radius $\tilde{r}$, disk half-thickness $\tilde{H}$, and radial velocity u using the relations

$$\tilde{r} \equiv \frac{r}{R_g}, \quad \tilde{H} \equiv \frac{H}{R_g}, \quad u \equiv \frac{\upsilon_r}{c}. \tag{17}$$

We showed in Paper I that the hot inner region of the disk has a wedge shape, so that

$$\tilde{H} = \hat{b}\tilde{r}, \qquad \hat{b} = \cot\Psi, \tag{18}$$

where the slope parameter $\hat{b}$ is an order-unity constant and Ψ is the opening angle of the disk (see Figure 1). Furthermore, we established that Equation (41) is separable in the spatial variable $\tilde{r}$ and the energy variable χ if the dimensionless velocity u has the form

$$u(\tilde{r}) = -\hat{u}\sqrt{\frac{GM}{c^2 r}} = -\hat{u}\, \tilde{r}^{-1/2}, \qquad \hat{u} > 0. \tag{19}$$

Interestingly, this velocity profile corresponds closely to that obtained in the self-similar ADAF disk model developed by R. D. Blandford & M. C. Begelman (1999).

For the radio-quiet AGNs that we consider here, outflows do not occur in the hot inner region, and therefore we can combine Equation (19) with Equations (19), (20), and (21) from R. D. Blandford & M. C. Begelman (1999) to conclude that the Shakura–Sunyaev viscosity parameter, $\alpha_{\rm SS}$, is given by

$$\alpha_{SS} = \frac{15\hat{u}(2\lambda_{ss} - \sqrt{6\epsilon_{ss} + \lambda_{ss}^2})}{2[6\epsilon_{ss} - 9 + 2\lambda_{ss}(\lambda_{ss} + \sqrt{6\epsilon_{ss} + \lambda_{ss}^2})]}, \tag{20}$$

where λ_{ss} and ϵ_{ss} denote the dimensionless angular momentum and energy transport rates in the disk. We refer the reader to R. D. Blandford & M. C. Begelman (1999) for a complete discussion of the parameters λ_{ss} and ϵ_{ss}. As demonstrated in Paper I, the Mach number, $\mathscr{M} = |v_r|/a$, obtained in our model is given by

$$\mathscr{M} = \hat{u}\left\{\frac{2}{5}\left[1 - \frac{1}{9}\left(\lambda_{ss} + \sqrt{\lambda_{ss}^2 + 6\epsilon_{ss}}\right)^2\right]\right\}^{-1/2}. \tag{21}$$

Equations (19), (20), and (21) describe the structure of an ADAF disk, with $\dot{m} \ll 1$. However, the accretion flows studied here are likely to have higher accretion rates, corresponding to the LHAF mode of accretion, with $\dot{m} \sim 1$ (F. Yuan 1999, 2001). Nonetheless, we argue that the above relations still provide a useful approximation of the disk structure in the case of LHAF accretion. The argument is based on the observation that, in the simulations carried out by F. Yuan (1999, 2001), the surface density of the disk, $\Sigma = \rho H$, varies as a power law in radius, with $\Sigma \propto r^{-p}$, where the index p is in the range $1/2 < p < 1$. Based on the mass conservation relation (Equation (6)), we therefore conclude that the radial velocity profile is given by

$$u(\tilde{r}) \propto \tilde{r}^{p-1}. \tag{22}$$

We therefore conclude that the velocity profile in the LHAF disk is reasonably approximated by the freefall profile given by Equation (19).

2.4. Density and Optical Depth Distribution

We assume here that the accreting gas is composed of fully ionized hydrogen, so that Equation (6) becomes

$$\dot{M} = 4\pi|v_r|rHm_p n_e = 4\pi c|u|R_g^2\tilde{r}\tilde{H}m_p n_e. \tag{23}$$

We can also rewrite the dimensionless accretion rate $\dot{m}$ in the form (see Equation (12))

$$\dot{m} = \frac{\dot{M}}{\dot{M}_{\rm E}} = \eta_{\rm bol}|u|\tilde{r}\tilde{H}n_e\sigma_{\rm T}R_g. \tag{24}$$

The electron number density, n_e, can be computed by combining Equations (18), (19), and (24), which yields

$$n_e(\tilde{r}) = \frac{\dot{m}}{\eta_{\rm bol}|u|\tilde{r}\tilde{H}\sigma_{\rm T}R_g} = \frac{\dot{m}\tilde{r}^{-3/2}}{\eta_{\rm bol}\hat{u}\hat{b}R_g\sigma_{\rm T}}, \tag{25}$$

from which it follows that the spatial diffusion coefficient, κ_ℓ, can be expressed as

$$\kappa_\ell(\tilde{r}) \equiv \frac{c\ell}{3} = \frac{\eta_{\rm bol}\hat{u}\hat{b}cR_g\tilde{r}^{3/2}}{3\dot{m}}, \tag{26}$$

where $\ell = (n_e\sigma_{\rm T})^{-1}$ is the electron scattering mean free path.

The transport of the radiation in the radial direction is heavily influenced by electron scattering, and therefore it is convenient to transform the spatial variable from the dimensionless radius, $\tilde{r}$, to the electron scattering optical depth, τ. The resulting transformation is given by

$$d\tau = n_e\sigma_{\rm T}\,dr = n_e\sigma_{\rm T}R_g\,d\tilde{r} \quad = \frac{\dot{m}\tilde{r}^{-3/2}\,d\tilde{r}}{\eta_{\rm bol}\hat{u}\hat{b}}, \tag{27}$$

where we have obtained the final result by using Equation (25) to substitute for the electron number density, n_e. This relation can be integrated to show that

$$\tau(\tilde{r}) = \frac{2\dot{m}}{\eta_{\rm bol}\hat{u}\hat{b}}\left(\tilde{r}_{\rm in}^{-1/2} - \tilde{r}^{-1/2}\right), \tag{28}$$

where τ is measured from the inner surface of the wedge flow region, at radius $r_{\rm in}$, outward to radius r. The scattering optical depths at the inner and outer boundaries, $\tau_{\rm in}$ and $\tau_{\rm out}$, respectively, are defined by

$$\tau_{\rm in} \equiv \tau(\tilde{r}_{\rm in}) = 0, \qquad \tau_{\rm out} \equiv \tau(\tilde{r}_{\rm out}). \tag{29}$$

We can also use Equation (28) to solve for the dimensionless radius $\tilde{r}$ as a function of the scattering optical depth τ, which yields

$$\tilde{r}(\tau) = \left(\tilde{r}_{\rm in}^{-1/2} - \frac{\eta_{\rm bol}\hat{u}\hat{b}\tau}{2\dot{m}}\right)^{-2}. \tag{30}$$

This relation will prove useful once we transform the spatial variable in the transport equation from $\tilde{r}$ to τ in Section 2.8.

2.5. Transport Equation

The photon distribution function $f(\boldsymbol{r}, \epsilon, t)$ is described by the general time-dependent radiation transport equation (P. A. Becker 2003):

$$\frac{\partial f}{\partial t} = -\boldsymbol{v}\cdot\boldsymbol{\nabla}f + \boldsymbol{\nabla}\cdot(\kappa_\ell\boldsymbol{\nabla}f) + (\boldsymbol{\nabla}\cdot\boldsymbol{v})\frac{\epsilon}{3}\frac{\partial f}{\partial\epsilon} + \frac{n_e\sigma_{\rm T}c}{m_ec^2}\frac{1}{\epsilon^2}\frac{\partial}{\partial\epsilon}\left[\epsilon^4\left(f + k_{\rm B}T_e\frac{\partial f}{\partial\epsilon}\right)\right] + Q, \tag{31}$$

where $\boldsymbol{v}$ denotes the velocity of the accreting plasma, κ_ℓ is the spatial diffusion coefficient, ϵ is the energy of photons, n_e is the number density of electrons, $\sigma_{\rm T}$ refers to the Thomson cross section, $k_{\rm B}$ is the Boltzmann constant, T_e is the electron temperature, m_e is the electron mass, and c is the speed of light. The term Q refers to the source term for any seed photons which is normalized so that the quantity $\epsilon^2Q(\boldsymbol{r}, \epsilon, t)\,d\epsilon$ equals the number of seed photons injected at radius $\boldsymbol{r}$ per unit volume per unit time with energy between ϵ and $\epsilon + d\epsilon$. The photon distribution function f is also normalized so that the number density n_r and energy density U_r of photons are expressed by

$$n_r(\boldsymbol{r}, t) = \int_0^\infty \epsilon^2 f(\boldsymbol{r}, \epsilon, t)\,d\epsilon \;\propto\; {\rm cm^{-3}},$$
$$U_r(\boldsymbol{r}, t) = \int_0^\infty \epsilon^3 f(\boldsymbol{r}, \epsilon, t)\,d\epsilon \;\propto\; {\rm erg\,cm^{-3}}. \tag{32}$$

Working in cylindrical coordinates and assuming the injection of monochromatic seed photons, T. Le & P. A. Becker (2005) showed that the vertical average of Equation (31) is given by

$$\frac{\partial f_{\rm G}}{\partial t} + v_r \frac{\partial f_{\rm G}}{\partial r} = \frac{1}{3rH}\frac{\partial}{\partial r}(rHv_r)\,\epsilon\,\frac{\partial f_{\rm G}}{\partial \epsilon} + \frac{1}{rH}\frac{\partial}{\partial r}\left(rH\kappa_\ell \frac{\partial f_{\rm G}}{\partial r}\right) - \frac{f_{\rm G}}{t_{\rm esc}} + \frac{n_e\sigma_{\rm T}c}{m_e c^2\epsilon^2}\frac{\partial}{\partial \epsilon}\left[\epsilon^4\left(f_{\rm G} + k_{\rm B}T_e\frac{\partial f_{\rm G}}{\partial \epsilon}\right)\right] + \frac{N_*\delta(r-r_*)\delta(\epsilon-\epsilon_*)\delta(t-t_*)}{4\pi r_* H_* \epsilon_*^2}, \tag{33}$$

where $f_{\rm G}(N_*, r, r_*, \epsilon, \epsilon_*, t, t_*)$ refers to the Green's function describing the impulsive injection of N_* seed photons with energy ϵ_* from a source located at radius r_* at time t_*. The quantities $t_{\rm esc}(r)$, $H(r)$, $v_r(r)$, and $\kappa_\ell(r)$ denote the mean time for photons to escape through the face of the disk, the disk half-thickness, the radial inflow velocity, and the spatial diffusion coefficient for the radiation at radius r, respectively, and $H_* = H(r_*)$.

2.6. Photon Source Distribution

The particular solution, $f(r, \epsilon, t)$, associated with the general source term Q is related to the Green's function $f_{\rm G}$ in cylindrical coordinates by the integral convolution

$$f(r, \epsilon, t) = \int_0^\infty \int_0^\infty \int_0^\infty \frac{f_{\rm G}(N_*, r, r_*, \epsilon, \epsilon_*, t, t_*)}{N_*} \times \epsilon_*^2\, Q(r_*, \epsilon_*, t_*)\, 4\pi r_*\, H(r_*)\, dr_*\, d\epsilon_*\, dt_*. \tag{34}$$

In the scenario considered here, an initial burst of fluorescent iron K and L seed photons is injected at time t_1 at the inner injection radius r_1, due to iron photoionization, which is driven by a flash of X-rays from the hot inner corona. The X-rays result from the upscattering of soft UV photons by high-energy electrons accelerated by impulsive reconnection in the corona (J. Malzac & E. Jourdain 2000; A. Zoghbi et al. 2010; D. R. Wilkins et al. 2016, 2022). This event is followed at a later time t_2 by another burst of iron K and L seed photons that occurs at the outer injection radius r_2, which is powered by a pressure wave propagating outward from the first burst. Due to the linearity of the transport equation (Equation (33)), one can treat the combined effect from the two coupled bursts by adding the source terms together. The general source function Q associated with the entire scenario can therefore be written in the form

$$Q(r_*, \epsilon_*, t_*) = \frac{N_{\rm K1}\delta(r_*-r_1)\delta(\epsilon_*-\epsilon_{\rm K})\delta(t_*-t_1)}{4\pi r_1 H_1 \epsilon_{\rm K}^2} + \frac{N_{\rm L1}\delta(r_*-r_1)\delta(\epsilon_*-\epsilon_{\rm L})\delta(t_*-t_1)}{4\pi r_1 H_1 \epsilon_{\rm L}^2} + \frac{N_{\rm K2}\delta(r_*-r_2)\delta(\epsilon_*-\epsilon_{\rm K})\delta(t_*-t_2)}{4\pi r_2 H_2 \epsilon_{\rm K}^2} + \frac{N_{\rm L2}\delta(r_*-r_2)\delta(\epsilon_*-\epsilon_{\rm L})\delta(t_*-t_2)}{4\pi r_2 H_2 \epsilon_{\rm L}^2}, \tag{35}$$

where the first two terms describe the inner, first injection event at (r_1, t_1) and the final two terms describe the subsequent, outer injection event at (r_2, t_2). In the scenario considered here, the time delay between the two injection events, $t_2 - t_1$, is equal to the sound propagation time between radius r_1 and radius r_2, as discussed in Section 2.12. Because the transport equation (33) is linear, the distribution function $f(r, \epsilon, t)$ is equal to the superposition of the Green's functions corresponding to the four source terms in Equation (35). We can therefore write the general solution in the form

$$f(r, \epsilon, t) = f_{\rm G}(N_{\rm K1}, r, r_1, \epsilon, \epsilon_{\rm K}, t, t_1) + f_{\rm G}(N_{\rm L1}, r, r_1, \epsilon, \epsilon_{\rm L}, t, t_1) + f_{\rm G}(N_{\rm K2}, r, r_2, \epsilon, \epsilon_{\rm K}, t, t_2) + f_{\rm G}(N_{\rm L2}, r, r_2, \epsilon, \epsilon_{\rm L}, t, t_2). \tag{36}$$

The function $f(r, \epsilon, t)$ represents the total photon distribution inside the wedge region of the accretion disk, resulting from the four individual injection events. The modular form of this equation allows us to obtain the solution for $f(r, \epsilon, t)$ using the same methods employed in Paper I to solve for the Green's function $f_{\rm G}$.

2.7. Fourier Transformation

In order to generate theoretical predictions for the Fourier time lags, it is convenient to work directly in Fourier space. We therefore transform the transport equation by applying the operator $\int_{-\infty}^{\infty} e^{i\omega t}\, dt$ to Equation (33). This yields (see Paper I)

$$-i\omega F_{\rm G} + v_r \frac{\partial F_{\rm G}}{\partial r} = \frac{1}{3rH}\frac{\partial}{\partial r}(rHv_r)\,\epsilon\,\frac{\partial F_{\rm G}}{\partial \epsilon} + \frac{1}{rH}\frac{\partial}{\partial r}\left(rH\kappa_\ell \frac{\partial F_{\rm G}}{\partial r}\right) - \frac{F_{\rm G}}{t_{\rm esc}} + \frac{n_e\sigma_{\rm T}c}{m_e c^2\epsilon^2}\frac{\partial}{\partial \epsilon}\left[\epsilon^4\left(F_{\rm G} + k_{\rm B}T_e\frac{\partial F_{\rm G}}{\partial \epsilon}\right)\right] + \frac{N_*\delta(r-r_*)\delta(\epsilon-\epsilon_*)e^{i\omega t_*}}{4\pi r_* H_* \epsilon_*^2}, \tag{37}$$

where the angular Fourier frequency $\omega = 2\pi\nu_{\rm F}$, and the Fourier transform of the Green's function, denoted by $F_{\rm G}$, is defined by

$$F_{\rm G}(r, r_*, \epsilon, \epsilon_*, \omega, t_*) \equiv \int_{-\infty}^{\infty} e^{i\omega t} f_{\rm G}(r, r_*, \epsilon, \epsilon_*, t, t_*)\, dt. \tag{38}$$

In analogy with Equation (36), we find that the total Fourier transform of the photon distribution inside the disk resulting from the four seed photon injection events is given by

$$F(r, \epsilon, \omega) = F_{\rm G}(N_{\rm K1}, r, r_1, \epsilon, \epsilon_{\rm K}, \omega, \omega_1) + F_{\rm G}(N_{\rm L1}, r, r_1, \epsilon, \epsilon_{\rm L}, \omega, \omega_1) + F_{\rm G}(N_{\rm K2}, r, r_2, \epsilon, \epsilon_{\rm K}, \omega, \omega_2) + F_{\rm G}(N_{\rm L2}, r, r_2, \epsilon, \epsilon_{\rm L}, \omega, \omega_2). \tag{39}$$

The linear form of Equation (39) indicates that we only need to obtain the solution for the Green's function Fourier transform, $F_{\rm G}$, in order to calculate the total Fourier transform, F, for the two coupled bursts. The general solution for the Green's function, $F_{\rm G}$, was worked out in Paper I, and we present a summary of the derivation below.

2.8. Green's Function Solution

Following the analysis in Paper I, we introduce the dimensionless Fourier frequency $\tilde{\omega}$, time q, temperature Θ, and photon energy χ, given by

$$\tilde{\omega} \equiv \frac{R_g}{c}\omega,\ q \equiv \frac{c}{R_g}t,\ \Theta \equiv \frac{k_{\rm B}T_e}{m_e c^2},\ \chi \equiv \frac{\epsilon}{k_{\rm B}T_e} = \frac{\epsilon}{\Theta m_e c^2}. \tag{40}$$

Utilizing these dimensionless relations, along with Equations (17), (19), and (25), the transport equation (Equation (37)) now becomes

$$\begin{aligned} -i\frac{c\tilde{\omega}F_{\rm G}}{R_g} - \frac{c\hat{u}\tilde{r}^{-1/2}}{R_g}\frac{\partial F_{\rm G}}{\partial \tilde{r}} &= \frac{c\hat{u}}{3R_g\tilde{r}\tilde{H}}\frac{\partial}{\partial \tilde{r}}(\tilde{H}\tilde{r}^{1/2})\chi\frac{\partial F_{\rm G}}{\partial \chi} \\ &+ \frac{1}{R_g^2\tilde{r}\tilde{H}}\frac{\partial}{\partial \tilde{r}}\left(\tilde{r}\tilde{H}\kappa_\ell\frac{\partial F_{\rm G}}{\partial \tilde{r}}\right) - \frac{F_{\rm G}}{t_{\rm esc}} \\ &+ \frac{\Theta c\dot{m}\tilde{r}^{-1/2}}{\eta_{\rm bol}\hat{u}\tilde{H}R_g\chi^2}\frac{\partial}{\partial\chi}\left[\chi^4\left(F_{\rm G} + \frac{\partial F_{\rm G}}{\partial\chi}\right)\right] \\ &+ \frac{N_*\delta(\tilde{r}-\tilde{r}_*)\delta(\chi-\chi_*)e^{i\tilde{\omega}q_*}}{4\pi R_g^3\tilde{r}_*\tilde{H}_*\Theta^3(m_e c^2)^3{\chi_*}^2}, \end{aligned} \tag{41}$$

where the mean escape timescale, $t_{\rm esc}$, for photons diffusing out through the upper and lower surfaces of the disk is given by

$$t_{\rm esc}(\tilde{r}) = \frac{H}{v_{\rm diff\perp}} = \frac{H}{{\rm Min}(c/\tau_\perp,\ c)} = {\rm Max}(\tau_\perp,\ 1)\frac{H}{c}. \tag{42}$$

Here, $v_{\rm diff\perp}$ represents the vertical photon diffusion velocity, which is computed using

$$v_{\rm diff\perp}(\tilde{r}) = {\rm Min}\left(\frac{c}{\tau_\perp},\ c\right), \tag{43}$$

where $\tau_\perp$ is the perpendicular scattering optical thickness of the disk, which is related to $\tilde{r}$ via

$$\tau_\perp(\tilde{r}) = \frac{H}{\ell} = Hn_e\sigma_{\rm T} = \frac{\dot{m}\tilde{r}^{-1/2}}{\eta_{\rm bol}\hat{u}}. \tag{44}$$

The optical thickness of the disk with respect to electron scattering, $\tau_\perp$, in the vertical direction is distinct from the optical depth in the radial direction in the equatorial plane, τ. Equations (18), (42), and (44) can be combined to obtain

$$t_{\rm esc}(\tilde{r}) = \frac{\hat{b}\tilde{r}R_g}{c}{\rm Max}\left(\frac{\dot{m}\tilde{r}^{-1/2}}{\eta_{\rm bol}\hat{u}},\ 1\right). \tag{45}$$

It is convenient to transform the radial variable in the transport equation (Equation (41)) from $\tilde{r}$ to the scattering optical depth, τ, using Equations (26), (27), and (30), which yields, after simplification,

$$\begin{aligned} -i\tilde{\omega}\frac{\eta_{\rm bol}\hat{u}\hat{b}\tilde{r}^{3/2}}{\dot{m}}F_{\rm G} - \hat{u}\tilde{r}^{-1/2}\frac{\partial F_{\rm G}}{\partial\tau} &= -\frac{\eta_{\rm bol}\hat{u}^2\hat{b}}{2\dot{m}}\chi\frac{\partial F_{\rm G}}{\partial\chi} \\ &+ \frac{2\eta_{\rm bol}\hat{u}\hat{b}\tilde{r}^{1/2}}{3\dot{m}}\frac{\partial F_{\rm G}}{\partial\tau} + \frac{1}{3}\frac{\partial^2 F_{\rm G}}{\partial\tau^2} - \frac{R_g F_{\rm G}}{ct_{\rm esc}}\frac{\eta_{\rm bol}\hat{u}\hat{b}\tilde{r}^{3/2}}{\dot{m}} \\ &+ \frac{\Theta}{\chi^2}\frac{\partial}{\partial\chi}\left[\chi^4\left(F_{\rm G} + \frac{\partial F_{\rm G}}{\partial\chi}\right)\right] \\ &+ \frac{N_*\delta(\tau-\tau_*)\delta(\chi-\chi_*)e^{i\tilde{\omega}q_*}}{4\pi cR_g^2\tilde{r}_*^2\hat{b}\Theta^3(m_e c^2)^3{\chi_*}^2}. \end{aligned} \tag{46}$$

We can now use Equation (45) to substitute $t_{\rm esc}$ in Equation (46), obtaining

$$\begin{aligned} -i\tilde{\omega}\frac{\eta_{\rm bol}\hat{u}\hat{b}\tilde{r}^{3/2}}{\dot{m}}F_{\rm G} - \hat{u}\tilde{r}^{-1/2}\frac{\partial F_{\rm G}}{\partial\tau} &= -\frac{\eta_{\rm bol}\hat{u}^2\hat{b}}{2\dot{m}}\chi\frac{\partial F_{\rm G}}{\partial\chi} \\ &+ \frac{2\eta_{\rm bol}\hat{u}\hat{b}\tilde{r}^{1/2}}{3\dot{m}}\frac{\partial F_{\rm G}}{\partial\tau} + \frac{1}{3}\frac{\partial^2 F_{\rm G}}{\partial\tau^2} \\ &- \frac{\eta_{\rm bol}\hat{u}\tilde{r}^{1/2}}{\dot{m}}{\rm Min}\left(\frac{\eta_{\rm bol}\hat{u}\tilde{r}^{1/2}}{\dot{m}},\ 1\right)F_{\rm G} \\ &+ \frac{\Theta}{\chi^2}\frac{\partial}{\partial\chi}\left[\chi^4\left(F_{\rm G} + \frac{\partial F_{\rm G}}{\partial\chi}\right)\right] \\ &+ \frac{N_*\delta(\tau-\tau_*)\delta(\chi-\chi_*)e^{i\tilde{\omega}q_*}}{4\pi cR_g^2\tilde{r}_*^2\hat{b}\Theta^3(m_e c^2)^3{\chi_*}^2}, \end{aligned} \tag{47}$$

where $\tilde{r}$ is a function of τ via Equation (30). Equation (47) is the fundamental partial differential equation satisfied by the Green's function Fourier transform, $F_{\rm G}$, which describes the radiation distribution inside the wedge-shaped region of the accretion disk, and therefore it is the starting point for the subsequent analysis, which leads to the solution for $F_{\rm G}$.

2.9. Orthogonal Expansion

The analytical solution for the Fourier transform, $F_{\rm G}$, can be expressed in terms of the separation functions

$$F_\lambda(\chi,\ \tau,\ \tilde{\omega}) = \mathcal{G}(\tau,\ \tilde{\omega})\,\mathcal{H}(\chi,\ \tilde{\omega}), \tag{48}$$

where λ represents the separation constant and $\mathcal{G}$ and $\mathcal{H}$ denote the spatial and energy separation functions, respectively. The exact solution for the Green's function $F_{\rm G}$ for each Fourier frequency $\tilde{\omega}$ can be obtained by introducing the series expansion

$$\begin{aligned} &F_{\rm G}(\tau,\ \tau_*,\ \chi,\ \chi_*,\ \tilde{\omega},\ q_*) \\ &\quad = \sum_{n=0}^{\infty} C_n(\tau_*,\ \chi_*,\ q_*)\,\mathcal{G}_n(\tau,\ \tilde{\omega})\,\mathcal{H}_n(\chi,\ \tilde{\omega}), \end{aligned} \tag{49}$$

where C_n, $\mathcal{G}_n$, and $\mathcal{H}_n$ denote the expansion coefficients and the spatial and energy eigenfunctions, respectively, which are obtained by solving Equation (47), combined with suitable physical boundary conditions. We can obtain the ordinary differential equations satisfied by the functions $\mathcal{G}$ and $\mathcal{H}$ by substituting Equation (48) into Equation (47) and rearranging the terms. The resulting, separated equation can be expressed as

$$\begin{aligned}&\frac{\eta_{\rm bol}\hat{u}\tilde{r}^{1/2}}{\dot{m}}{\rm Min}\left(\frac{\eta_{\rm bol}\hat{u}\tilde{r}^{1/2}}{\dot{m}},1\right)-i\frac{\tilde{\omega}\eta_{\rm bol}\hat{u}\hat{b}\tilde{r}^{3/2}}{\dot{m}}\\&-\frac{\hat{u}\tilde{r}^{-1/2}}{\mathcal{G}}\frac{d\mathcal{G}}{d\tau}-\frac{2\eta_{\rm bol}\hat{u}\hat{b}\tilde{r}^{1/2}}{3\dot{m}\mathcal{G}}\frac{\partial\mathcal{G}}{\partial\tau}-\frac{1}{3\mathcal{G}}\frac{\partial^2\mathcal{G}}{\partial\tau^2}\\&=-\frac{\eta_{\rm bol}\hat{u}^2\hat{b}}{2\dot{m}\mathcal{H}}\chi\frac{d\mathcal{H}}{d\chi}+\frac{\Theta}{\chi^2\mathcal{H}}\frac{d}{d\chi}\left[\chi^4\left(\mathcal{H}+\frac{d\mathcal{H}}{d\chi}\right)\right]\\&=\frac{\eta_{\rm bol}\hat{u}^2\hat{b}}{2\dot{m}}\lambda,\end{aligned}\tag{50}$$

where the right-hand side is a constant, and is therefore independent of both χ and τ.

We can now decouple Equation (50) into two separate ordinary differential equations satisfied by the energy and spatial separation functions. The spatial-dependent separation function is given by

$$\begin{aligned}&\frac{d^2\mathcal{G}}{d\tau^2}+\left[2\frac{\eta_{\rm bol}\hat{u}\hat{b}}{\dot{m}}\tilde{r}^{1/2}+3\hat{u}\tilde{r}^{-1/2}\right]\frac{d\mathcal{G}}{d\tau}+\frac{3\eta_{\rm bol}\hat{u}}{\dot{m}}\\&\times\left[i\hat{b}\tilde{\omega}\tilde{r}^{3/2}-\tilde{r}^{1/2}{\rm Min}\left(\frac{\eta_{\rm bol}\hat{u}\tilde{r}^{1/2}}{\dot{m}},1\right)+\frac{\hat{u}\hat{b}}{2}\lambda\right]\mathcal{G}=0,\end{aligned}\tag{51}$$

where $\tilde{r}$ is a function of τ via Equation (30). The corresponding energy-dependent separation equation is given by

$$\frac{1}{\chi^2}\frac{d}{d\chi}\left[\chi^4\left(\mathcal{H}+\frac{d\mathcal{H}}{d\chi}\right)\right]-\delta\chi\frac{d\mathcal{H}}{d\chi}-\delta\lambda\mathcal{H}=0,\tag{52}$$

where we have introduced the new parameter δ, defined by

$$\delta\equiv\frac{\eta_{\rm bol}\hat{u}^2\hat{b}}{2\dot{m}\Theta},\tag{53}$$

which is a global constant in our model.

2.10. Solutions to the Separation Equations

The spatial separation equation (Equation (51)) in τ space can be solved by imposing free-streaming boundary conditions at the inner and outer radii of the hot inner region. We employ a bidirectional method for integrating Equation (51) in order to determine the spatial eigenfunctions $\mathcal{G}_n(\tau)$ and the corresponding eigenvalues λ_n that satisfy both the inner and outer boundary conditions. It is important to note that because of the appearance of the Fourier frequency, $\tilde{\omega}$, in Equation (51), it follows that we will obtain a distinct set of eigenvalues, λ_n, for each value of the Fourier frequency. The set of spatial eigenfunctions we obtain is verified by confirming the orthogonality between any pair of eigenfunctions $\mathcal{G}_m(\tau)$ and $\mathcal{G}_n(\tau)$ using the integral

$$\int_0^{\tau_{\rm out}}\Omega_w(\tau)\mathcal{G}_m(\tau)\mathcal{G}_n(\tau)\quad d\tau=0,\quad\lambda_m\neq\lambda_n,\tag{54}$$

where λ_n and λ_m are distinct eigenvalues corresponding to $\mathcal{G}_n(\tau)$ and $\mathcal{G}_m(\tau)$, respectively. The function $\Omega_w(\tau)$ and Equation (54) represent the weight function for the spatial eigenfunctions, given by (see Paper I)

$$\Omega_w(\tau)=\frac{3\eta_{\rm bol}\hat{u}^2\hat{b}\tilde{r}^2}{\dot{m}}\exp\left[\frac{3\dot{m}}{\eta_{\rm bol}\hat{b}}\left(\tilde{r}_{\rm in}^{-1}-\tilde{r}^{-1}\right)\right],\tag{55}$$

where $\tilde{r}$ is, again, a function of the optical depth τ via Equation (30).

The spatial eigenfunctions $\mathcal{G}_n(\tau)$ do not have a closed-form expression, but the energy eigenfunctions $\mathcal{H}_n(\tau)$ can be determined analytically by solving the energy separation equation (Equation (52)), which yields (P. A. Becker 2003)

$$\mathcal{H}_n(\chi)=\begin{cases}\chi^{\kappa-4}e^{-\chi/2}W_{\kappa,\mu}(\chi_*)M_{\kappa,\mu}(\chi), & \chi\leqslant\chi_*,\\ \chi^{\kappa-4}e^{-\chi/2}M_{\kappa,\mu}(\chi_*)W_{\kappa,\mu}(\chi), & \chi\geqslant\chi_*,\end{cases}\tag{56}$$

where $M_{\kappa,\mu}$ and $W_{\kappa,\mu}$ represent the Whittaker functions, and the indices κ and μ are defined by (M. Abramowitz et al. 1988)

$$\kappa\equiv\frac{1}{2}(\delta+4),\qquad\mu\equiv\frac{1}{2}[(3-\delta)^2+4\delta\lambda_n]^{1/2}.\tag{57}$$

Once we have obtained the sets of eigenfunctions $\mathcal{G}_n$ and $\mathcal{H}_n$ and eigenvalues λ_n, we can continue to determine the corresponding set of expansion coefficients, C_n, for each Fourier frequency $\tilde{\omega}$. Following the procedure discussed in Paper I, we first evaluate the derivative jump condition at the dimensionless photon injection energy $\chi=\chi_*$. Next, we utilize the orthogonality of the spatial eigenfunctions as established in Equation (54) to solve for C_n, which after some manipulation yields

$$C_n=\frac{N_*\Omega_w(\tau_*)\mathcal{G}_n(\tau_*)e^{\chi_*/2}e^{i\tilde{\omega}q_*}\Gamma(\mu-\kappa+1/2)}{4\pi cR_g^2\tilde{r}_*^2\hat{b}\Theta^4(m_ec^2)^3{\chi_*}^{\kappa}\mathfrak{I}_n\Gamma(1+2\mu)},\tag{58}$$

where $\mathfrak{I}_n$ denotes the quadratic normalization integral, defined by

$$\mathfrak{I}_n\equiv\int_{\tau_{\rm in}}^{\tau_{\rm out}}\Omega_w(\tau)\,\mathcal{G}_n^2(\tau)\quad d\tau.\tag{59}$$

By combining Equations (49), (56), and (58), we can obtain the exact solution for the Green's function Fourier transform, $F_{\rm G}$, in the form of a mathematical expansion over the set of eigenvalues. The result obtained is

$$\begin{aligned}&F_{\rm G}(\tau_*,\tau,\chi_*,\chi,\tilde{\omega},q_*)=\frac{N_*\chi^{\kappa-4}\Omega_w(\tau_*)e^{(\chi_*-\chi)/2}e^{i\tilde{\omega}q_*}}{4\pi cR_g^2\tilde{r}_*^2\hat{b}\Theta^4(m_ec^2)^3{\chi_*}^{\kappa}}\\&\sum_{n=1}^{\infty}\frac{\Gamma(\mu-\kappa+1/2)}{\mathfrak{I}_n\Gamma(1+2\mu)}\mathcal{G}_n(\tau_*)\mathcal{G}_n(\tau)M_{\kappa,\mu}(\chi_{\rm min})W_{\kappa,\mu}(\chi_{\rm max}),\end{aligned}\tag{60}$$

where $\chi_{\rm min}\equiv\min(\chi,\chi_*)$ and $\chi_{\rm max}\equiv\max(\chi,\chi_*)$. We note that while the summation expressed here extends to $n=\infty$, sufficient convergence can be achieved for $n\sim20-30$ in practical calculations.

2.11. Simulation of Fourier-transformed Light Curves

Equation (60) gives the exact solution for the Fourier transform Green's function, $F_{\rm G}$, for each Fourier frequency $\tilde{\omega}$, and is one of the main results of Paper I, which we will now use to calculate the Fourier-transformed spectrum for the new coupled-burst model developed here. Here, we remind the reader that our disk source is anisotropic, meaning that the radiation field depends on the angle, θ, between the observer and the spin axis of the disk (see Figure 1). We define $\mathscr{F}(\epsilon, t, \theta)$ to be the flux distribution (count-rate spectrum) measured by an observer on Earth located at angle θ relative to the spin axis. The flux distribution is normalized so that $\mathscr{F}(\epsilon, t, \theta)\, d\epsilon\, dt$ gives the number of photons per unit area detected in the energy range between ϵ and $\epsilon + d\epsilon$ in time interval dt.

In our model, the disk is radiating separate components through the "side," the outer edge, and the "face," the upper and lower surfaces, of the hot inner region (see Figure 1), and therefore the total flux distribution is given by

$$\mathscr{F}(\epsilon, t, \theta) = \mathscr{F}_{\rm side}(\epsilon, t)\sin\theta + \mathscr{F}_{\rm face}(\epsilon, t)\cos\theta, \tag{61}$$

where $\mathscr{F}_{\rm side}$ and $\mathscr{F}_{\rm face}$ represent the spectral emission from the side and face of the wedge region, respectively. The Fourier transform of the total count-rate spectrum is computed using

$$\tilde{\mathscr{F}}(\epsilon, \omega, \theta) \equiv \int_{-\infty}^{+\infty} \mathscr{F}(\epsilon, t, \theta) e^{i\omega t} dt, \tag{62}$$

which is used to compute the observational time lag distribution, as discussed in Section 3.1. Applying the operator $\int_{-\infty}^{+\infty} e^{i\omega t} dt$ to Equation (61), we obtain

$$\tilde{\mathscr{F}}(\epsilon, \omega, \theta) = \tilde{\mathscr{F}}_{\rm side}(\epsilon, \omega)\sin\theta + \tilde{\mathscr{F}}_{\rm face}(\epsilon, \omega)\cos\theta, \tag{63}$$

where $\tilde{\mathscr{F}}_{\rm side}$ and $\tilde{\mathscr{F}}_{\rm face}$ denote the Fourier transforms of the count-rate spectra emitted from the side and face of the wedge region, respectively.

In order to make contact with our theoretical model, it is convenient to rewrite Equation (63) in terms of the dimensionless parameters $(\chi, \tilde{\omega}, \tau, q)$, which yields

$$\tilde{\mathscr{F}}(\chi, \tilde{\omega}, N_*, \tau_*, \chi_*, q_*, \theta) = \tilde{\mathscr{F}}_{\rm side}(\chi, \tilde{\omega}, N_*, \tau_*, \chi_*, q_*) \sin\theta + \tilde{\mathscr{F}}_{\rm face}(\chi, \tilde{\omega}, N_*, \tau_*, \chi_*, q_*)\cos\theta. \tag{64}$$

and

$$\begin{aligned} &\tilde{\mathscr{F}}_{\rm face}(\chi, \tilde{\omega}, N_*, \tau_*, \chi_*, q_*) \\ &= \frac{N_* \chi^{\kappa-2} \Omega_w(\tau_*) e^{(\chi_*-\chi)/2} e^{i\tilde{\omega} q_*}}{4\pi \tilde{r}_*^2 \quad \Theta^2 m_e c^2 \chi_*{}^{\kappa} D^2} \sum_{n=1}^{\infty} \frac{\Gamma(\mu - \kappa + 1/2)}{\Im_n \Gamma(1 + 2\mu)} \mathcal{G}_n(\tau_*) \\ &\times M_{\kappa,\mu}(\chi_{\rm min}) W_{\kappa,\mu}(\chi_{\rm max}) \int_0^{\tau_{\rm out}} \frac{\eta_{\rm bol} \hat{u} \tilde{r}^{5/2}}{\dot{m}} {\rm Min} \\ &\times \left(\frac{\eta_{\rm bol} \hat{u} \tilde{r}^{1/2}}{\dot{m}}, 1\right) \quad \mathcal{G}_n(\tau) \quad d\tau, \end{aligned} \tag{66}$$

respectively, where D represents the distance to the source. We note that these two expressions differ from the corresponding Equations (101) and (107) in Paper I due to a factor of R_g/c that was erroneously included in those two equations.

It should be emphasized that Equation (64) gives the Fourier transform of the observed flux resulting from a single burst of seed photons with injection parameters $(N_*, \tau_*, \chi_*, q_*)$. Since the transport equation (Equation (47)) is linear, it follows that the total Fourier transform for two separate bursts of iron K and L seed photons is given by the sum of the transforms for the individual monochromatic bursts. Hence, we can write the complete solution in the form

$$\begin{aligned} &\tilde{\mathscr{F}}_1(\chi, \tilde{\omega}, N_{\rm K1}, N_{\rm L1}, \chi_{\rm K1}, \chi_{\rm L1}, \tau_1, q_1) \\ &\quad = \tilde{\mathscr{F}}(\chi, \tilde{\omega}, N_{\rm K1}, \tau_1, \chi_{\rm K1}, q_1) \\ &\quad + \tilde{\mathscr{F}}(\chi, \tilde{\omega}, N_{\rm L1}, \tau_1, \chi_{\rm L1}, q_1), \end{aligned} \tag{67}$$

and

$$\begin{aligned} &\tilde{\mathscr{F}}_2(\chi, \tilde{\omega}, N_{\rm K2}, N_{\rm L2}, \chi_{\rm K2}, \chi_{\rm L2}, \tau_2, q_2) \\ &\quad = \tilde{\mathscr{F}}(\chi, \tilde{\omega}, N_{\rm K2}, \tau_2, \chi_{\rm K2}, q_2) \\ &\quad + \tilde{\mathscr{F}}(\chi, \tilde{\omega}, N_{\rm L2}, \tau_2, \chi_{\rm L2}, q_2), \end{aligned} \tag{68}$$

where $\tilde{\mathscr{F}}_1$ and $\tilde{\mathscr{F}}_2$ refer to the first (inner) burst and the second (outer) burst, respectively, including the injection of both the K and L seed photons. Hence, the total Fourier transform of the photon count-rate spectrum, accounting for the injection of the K and L seed photons in the two X-ray bursts, can be written as

$$\begin{aligned} &\tilde{\mathscr{F}}_{\rm total}(\chi, \tilde{\omega}, N_{\rm K1}, N_{\rm L1}, N_{\rm K2}, N_{\rm L2}, \chi_{\rm K1}, \chi_{\rm L1}, \chi_{\rm K2}, \chi_{\rm L2}, \tau_1, \tau_2, q_1, q_2) \\ &\quad = \tilde{\mathscr{F}}_1(\chi, \tilde{\omega}, N_{\rm K1}, N_{\rm L1}, \chi_{\rm K1}, \chi_{\rm L1}, \tau_1, q_1) \\ &\quad + \tilde{\mathscr{F}}_2(\chi, \tilde{\omega}, N_{\rm K2}, N_{\rm L2}, \chi_{\rm K2}, \chi_{\rm L2}, \tau_2, q_2). \end{aligned} \tag{69}$$

The exact solutions for $\tilde{\mathscr{F}}_{\rm side}$ and $\tilde{\mathscr{F}}_{\rm face}$ are given by (see Paper I for complete details)

$$\begin{aligned} &\tilde{\mathscr{F}}_{\rm side}(\chi, \tilde{\omega}, N_*, \tau_*, \chi_*, q_*) \\ &= \frac{N_* \chi^{\kappa-2} \Omega_w(\tau_*) \tilde{r}_{\rm out}^2 e^{(\chi_*-\chi)/2} e^{i\tilde{\omega} q_*}}{4\pi \tilde{r}_*^2 \quad \Theta^2 m_e c^2 \chi_*{}^{\kappa} D^2} \sum_{n=1}^{\infty} \frac{\Gamma(\mu - \kappa + 1/2)}{\Im_n \Gamma(1 + 2\mu)} \\ &\times \mathcal{G}_n(\tau_*) \mathcal{G}_n(\tau_{\rm out}) M_{\kappa,\mu}(\chi_{\rm min}) W_{\kappa,\mu}(\chi_{\rm max}), \end{aligned} \tag{65}$$

This expression allows us to compute the Fourier transforms of the hard and soft X-ray light curves in order to make comparisons between our theory and the observational time lag data for specific sources. In our model, the two bursts are connected by the propagation of a pressure wave between the inner burst radius r_1 and the outer burst radius r_2. This is an important feature in our model, because the relative time delay due to the propagation of the sound wave, $\Delta t_{\rm prop}$, creates a phase shift between the Fourier transforms for the inner and outer bursts.

2.12. Propagation Time between Bursts

In our model, the complex behavior of the time lags as a function of the observational Fourier frequency ω results from an interaction between two coupled bursts of seed photons generated by partially ionized iron atoms located at two distinct radii in the accretion disk. The first burst results from the injection of iron K and L photons, which are produced by atoms that have been photoionized by a flash of X-rays from the hot inner corona, produced by energetic electrons accelerated in a transient reconnection event (J. Malzac & E. Jourdain 2000; P. Uttley et al. 2014). The first burst occurs at radius $r = r_1$ and time $t = t_1$. The thermal instability also produces a pressure wave that propagates outward at the speed of sound, until it encounters the standing shock located at the outer radius of the hot, wedge-shaped inner region of the accretion flow. At the shock location, the pressure wave dissipates, depositing its energy in the local gas. This triggers the production of bremsstrahlung emission that photoionizes the iron atoms, resulting in the injection of the second burst of fluorescent iron K and L photons, at radius $r = r_2$ and time $t = t_2$.

Because the pressure wave propagates at the speed of sound relative to the background gas, its speed relative to the frame of a stationary local observer is given by $v_{\rm prop}$, which we can compute using

$$v_{\rm prop} = a - |v_r| = \left(\frac{1}{\mathscr{M}} - 1\right)|v_r| = \left(\frac{1}{\mathscr{M}} - 1\right)\hat{u}c\tilde{r}^{-1/2}. \tag{70}$$

We note that in the hot, wedge-shaped inner region of the accretion disk treated here, the flow is subsonic, and therefore $v_{\rm prop} > 0$, implying the outward propagation of pressure waves. The propagation time, $\Delta t_{\rm prop}$, between the inner injection radius r_1 and the outer injection radius r_2 is therefore given by

$$\Delta t_{\rm prop} = \int_{r_1}^{r_2} \frac{dr}{v_{\rm prop}} = \frac{2R_g\left(\tilde{r}_2^{3/2} - \tilde{r}_1^{3/2}\right)}{3\hat{u}c\left(\frac{1}{\mathscr{M}} - 1\right)}, \tag{71}$$

where the final result follows from Equation (70). It is interesting to express the propagation time in units of the gravitational light-crossing time, R_g/c, which yields

$$\Delta q_{\rm prop} \equiv \Delta t_{\rm prop}\frac{c}{R_g} = \frac{2\left(\tilde{r}_2^{3/2} - \tilde{r}_1^{3/2}\right)}{3\hat{u}\left(\frac{1}{\mathscr{M}} - 1\right)}. \tag{72}$$

The evaluation of Equations (71) and (72) requires knowledge of the radial Mach number, $\mathscr{M}$, in the accreting plasma. In the self-similar disk structure assumed here, discussed in detail by R. D. Blandford & M. C. Begelman (1999), the Mach number has a global constant value throughout the disk. This value is given by Equation (49) of T. Mahapol & P. A. Becker (2024), which states that

$$\mathscr{M} = \hat{u}\left\{\frac{2}{5}\left[1 - \frac{1}{9}\left(\lambda_{\rm ss} + \sqrt{\lambda_{\rm ss}^2 + 6\epsilon_{\rm ss}}\right)^2\right]\right\}^{-1/2}, \tag{73}$$

where $\lambda_{\rm ss}$ and $\epsilon_{\rm ss}$ denote the dimensionless angular momentum and energy transport rates in the disk, respectively (R. D. Blandford & M. C. Begelman 1999). We typically find that $\lambda_{\rm ss} \approx 1/2$ and $\epsilon_{\rm ss} \approx 1/4$, in which case Equation (73) reduces to

$$\mathscr{M} \approx 2\,\hat{u}. \tag{74}$$

We can then express the propagation time $\Delta q_{\rm prop}$ in terms of the Mach number of the accreting plasma $\mathscr{M}$ as follows:

$$\Delta q_{\rm prop} \approx \frac{4}{3}\frac{\left(\tilde{r}_2^{3/2} - \tilde{r}_1^{3/2}\right)}{1 - 2\hat{u}}. \tag{75}$$

In our application to specific sources, we will allow the constants $\lambda_{\rm ss}$ and $\epsilon_{\rm ss}$ to vary as part of the procedure in which we use the coupled-burst model to fit the time lag data.

3. Time Lag Computation

In this section, we summarize the steps required for computing the X-ray time lags using the Fourier transforms of the hard and soft X-ray light curves, as discussed in Paper I. Some intermediate steps are skipped for brevity. We invite the reader to review Sections 1.1 and 4 of Paper I for a more in-depth explanation.

3.1. Time Lag Definition

As first suggested by M. van der Klis et al. (1987), the Fourier time lag, δt, at a selected observational Fourier frequency, ω, can be mathematically derived from the corresponding Fourier phase lag, ϕ, between the soft and hard Fourier-transformed X-ray light curves, using the expression

$$\phi(\omega) = {\rm Arg}[\mathfrak{S}^*(\omega)\mathfrak{H}(\omega)], \tag{76}$$

where the asterisk represents the complex conjugate, and $\mathfrak{S}(\omega)$ and $\mathfrak{H}(\omega)$ denote the Fourier-transformed soft and hard X-ray light curves, respectively. These quantities are computed from the corresponding soft and hard X-ray light curves, $\mathfrak{s}(t)$ and $\mathfrak{h}(t)$, respectively, using

$$\mathfrak{S}(\omega) = \int_{-\infty}^{+\infty} \mathfrak{s}(t)\, e^{i\omega t}dt,$$
$$\mathfrak{H}(\omega) = \int_{-\infty}^{+\infty} \mathfrak{h}(t)\, e^{i\omega t}dt. \tag{77}$$

Finally, we obtain the Fourier time lag, δt, which is computed from the Fourier phase lag, ϕ, using the definition (M. A. Nowak et al. 1999)

$$\delta t(\omega) \equiv \frac{\phi(\omega)}{\omega}. \tag{78}$$

According to the sign convention we adopt here, a positive value for δt represents a hard time lag. In this situation, the hard X-ray variability follows the soft variability at the angular Fourier frequency ω. The opposite case, $\delta t(\omega) < 0$, implies a soft time lag. It can be shown that if an exact time lag, Δt, is imposed between the hard light curve $\mathfrak{h}(t)$ and the soft light curve $\mathfrak{s}(t)$, such that $\mathfrak{h}(t + \Delta t) = \mathfrak{s}(t)$, then the resulting Fourier time lag is given by $\delta t(\omega) = \Delta t$, as expected (D. C. Baughman & P. A. Becker 2022).

3.2. Connection with X-Ray Light Curves

In connection with the theory developed here, we need to compute the functions $\mathfrak{S}(\omega)$ and $\mathfrak{H}(\omega)$ by evaluating Equation (69) at the soft and hard photon energies, ϵ_s and ϵ_h,

Table 1
Coupled-burst Model Free Parameter Values

Object	$\tilde{r}_{\rm out}$	$\tilde{r}_1$	$\tilde{r}_2$	θ (deg)	Ψ (deg)	$\eta_{\rm bol}$	$N_{\rm K2}/N_{\rm K1}$	$\mathscr{M}$	$k_{\rm B} T_e$ (keV)
1H 0707−495	100	38	98	48	59	0.443	1.59	0.705	8.69
Ark 564	100	42	86	36	55	0.498	3.03	0.717	18.91
NGC 4051	120	44	100	22	55	0.060	5.00	0.704	20.95
Mrk 766	120	26	114	40	59	0.249	2.38	0.742	10.22

respectively, and Fourier frequency ω. We remind the reader that the observational Fourier frequency, ω, is related to its dimensionless counterpart, $\tilde{\omega}$, by $\tilde{\omega} = \omega R_g/c$ (see Equation (40)). This implies that the set of dimensionless Fourier frequencies $\tilde{\omega}$ obtained from a given set of observational Fourier frequencies ω is a function of the black hole mass, M. The theory is expressed in terms of the dimensionless photon energies $\chi = \epsilon/(k_{\rm B} T_e)$, and the corresponding dimensionless soft and hard photon energies are therefore given by

$$\chi_s = \frac{\epsilon_s}{k_{\rm B} T_e}, \qquad \chi_h = \frac{\epsilon_h}{k_{\rm B} T_e}. \tag{79}$$

We can now use Equation (69) to evaluate the soft and hard photon energy Fourier transforms, which can be expressed as

$$\mathfrak{S}(\omega) \equiv \tilde{\mathscr{F}}_{\rm total}(\chi_s, \tilde{\omega}, N_{\rm K1}, N_{\rm L1}, N_{\rm K2}, N_{\rm L2}, \chi_{\rm K1}, \chi_{\rm L1}, \chi_{\rm K2}, \chi_{\rm L2}, \tau_1, \tau_2, q_1, q_2),$$
$$\mathfrak{H}(\omega) \equiv \tilde{\mathscr{F}}_{\rm total}(\chi_h, \tilde{\omega}, N_{\rm K1}, N_{\rm L1}, N_{\rm K2}, N_{\rm L2}, \chi_{\rm K1}, \chi_{\rm L1}, \chi_{\rm K2}, \chi_{\rm L2}, \tau_1, \tau_2, q_1, q_2). \tag{80}$$

Once we have selected values for all of the model parameters, Equation (78) enables us to compute the Fourier time lag for each value of the observational Fourier frequency ω. It is important to discuss the procedure for determining the model parameters, which we summarize here. In each case, we set the inner radius of the accretion disk using $r_{\rm in} = 1.61\, R_g$, which corresponds to a spin parameter $a = 0.98$ (see Paper I). The values of the black hole mass, M, and the bolometric luminosity ratio, $L_{\rm bol}/L_{\rm E}$, are determined using the observational estimates for each source, and this also yields the value of the dimensionless accretion rate, $\dot{m}$, since $\dot{m} = L_{\rm bol}/L_{\rm E}$ according to Equation (12). The values of the iron K and L photon injection energies, $\epsilon_{\rm K}$ and $\epsilon_{\rm L}$, are fixed at 6.4 keV and 0.89 keV, respectively (A. C. Fabian et al. 2009), and the value of the radial velocity parameter $\hat{u}$ is set to $0.25\sqrt{2}$ (Paper I), which is the expected value on the downstream side of the standing shock located at the outer boundary of the wedge-shaped inner region, which is the focus of our work here (S. Chakrabarti & L. G. Titarchuk 1995; S. K. Chakrabarti 1997a, 1997b).

3.3. Statistics for Iron Seed Photon Injection

It is important to quantify the number of iron K and L photons injected in the first and second bursts, denoted by $N_{\rm K1}$, $N_{\rm L1}$, $N_{\rm K2}$, and $N_{\rm L2}$. The first burst occurs in the hot inner region of the disk, where the plasma temperature reaches $T \sim 10^8$ K. The accreting material in this region is photoionized by a flash of X-rays from the even hotter corona, which contains populations of electrons heated by impulsive reconnection events up to temperature $T_e \sim 10^9$ K (D. R. Wilkins et al. 2022). The flash of X-rays removes electrons from the K shells of the iron atoms in the disk, resulting in a cascade that begins with the filling of the hole in the K shell by an electron dropping down from the L shell, which generates an iron K seed photon ~30% of the time, or the ejection of an Auger electron ~70% of the time (M. O. Krause 1979; J. S. Kaastra & R. Mewe 1993). The next step in the cascade is the filling of the hole in the L shell, which has a probability of $\sim 10^{-3}$ of resulting in the emission of an iron L seed photon versus the ejection of an Auger electron. Based on these statistical results, we set $N_{\rm L1} = 10^{-3} N_{\rm K1}$ for the inner burst. While the first burst of seed photons occurs in the hot plasma near the inner edge of the accretion disk, the outer burst occurs in the vicinity of the standing shock located at the outer edge of the wedge-shaped accretion region, where the temperature has an intermediate value between the hot phase and the much cooler UV-emitting outer region. Therefore, we assume that the photoionization to the K and L levels occurs with roughly equal probability for the outer burst, and therefore we set $N_{\rm L2} = N_{\rm K2}$. Hence, the relative strengths of the four seed photon injection events can be characterized by the ratio $N_{\rm K2}/N_{\rm K1}$, which is considered to be one of the free parameters in our model.

We can use the model to analyze the time lag data for a given source by varying the nine free parameters: the outer radius of the hot inner region $r_{\rm out}$, the injection radii of the first and second bursts r_1 and r_2, the number of iron K seed photons in the second burst $N_{\rm K2}$, the Mach number $\mathscr{M}$, the electron temperature T_e, the disk inclination angle θ, the disk opening angle Ψ, and the bolometric efficiency $\eta_{\rm bol}$. Once values are selected for all of the free parameters, we can apply the method developed in Section 2 to compute the theoretical X-ray time lags. The free parameter values are varied until adequate qualitative agreement is obtained with the time lag data for a given source. Specific applications to four NLS1 galaxies are presented in Section 4.

4. Applications to NLS1 Galaxies

Now that the time lag calculation procedure is established, we can utilize our theoretical formulation to analyze the X-ray Fourier time lags observed from four NLS1 galaxies. In this section, we apply the coupled-burst model developed in the previous sections to (1) 1H 0707–495, (2) Ark 564, (3) NGC 4051, and (4) Mrk 766. The results obtained will be compared with the model predictions from the single-burst

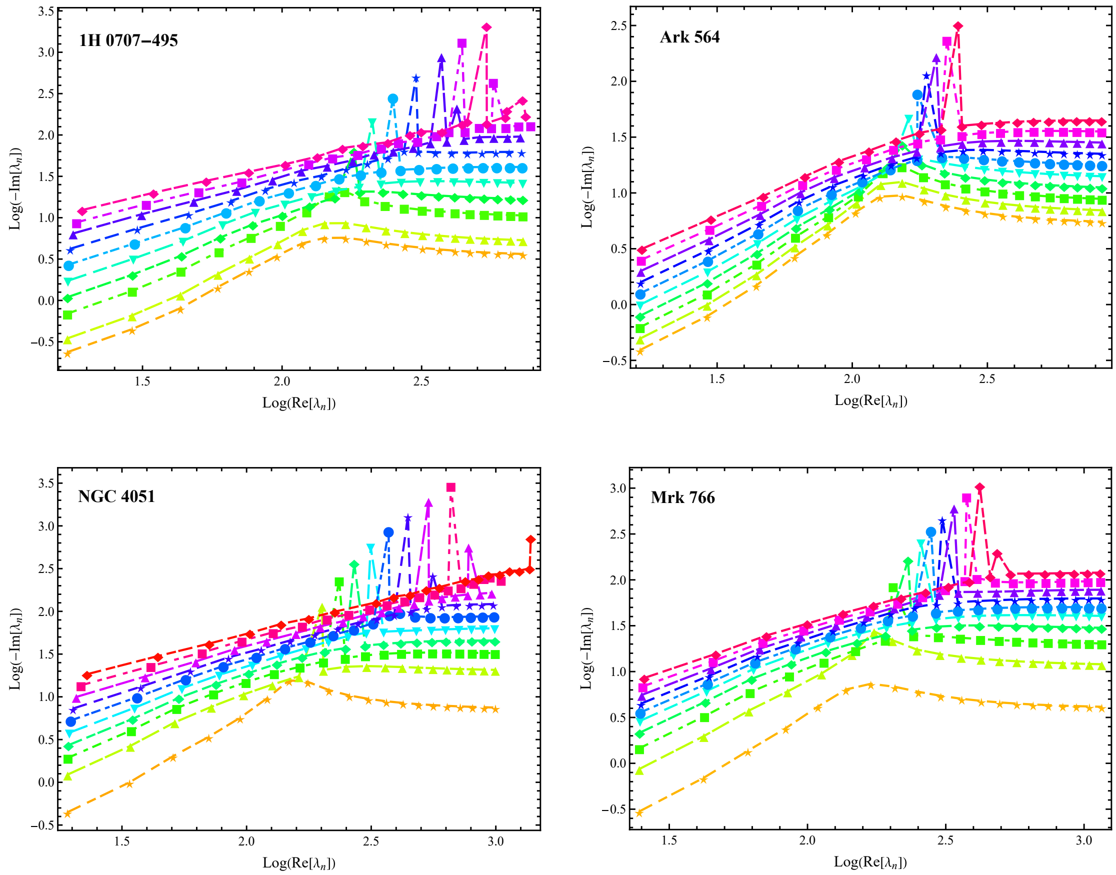

Figure 2. The complex-plane plots of the first 20 eigenvalues, λ_n, corresponding to each value of the dimensionless Fourier frequency, $\tilde{\omega}$, for 1H 0707−495 (top left), Ark 564 (top right), NGC 4051 (bottom left), and Mrk 766 (bottom right). A set of eigenvalues λ_n corresponding to the same $\tilde{\omega}$ are linked by the same dashed line and color. Each eigenvalue is represented by a plot marker. The eigenvalue index n increases from left to right while $\tilde{\omega}$ increases from bottom to top in the sequence.

model developed in Paper I. The model parameters can be found in Table 1.

4.1. 1H 0707−495

The first NLS1 source we consider as an initial application of our new model is 1H 0707−495, which is well known for its iron L variability and X-ray soft time lags. This source was analyzed by A. C. Fabian et al. (2012), who found that in its low, hard state, the spectrum displays a soft blackbody excess at 0–1 keV and a sharp drop at ∼7 keV, which is attributed to iron absorption. They modeled the 0.3–10 keV spectrum of 1H 0707−495 using blackbody emission with temperature $k_{\rm B}T_e \sim 0.3$–0.4 keV, combined with absorption, reflection, and relativistic blurring. The requirement of such a complex set of emission mechanisms to explain the formation process for the steady-state X-ray spectrum suggests that the underlying physics may not yet be completely understood.

The set of Fourier frequencies, $\nu_{\rm F}$, we use in our theoretical calculation for 1H 0707−495 is given by $\nu_{\rm F} \in \{5.41 \times 10^{-5}, 7.94 \times 10^{-5}, 1.58 \times 10^{-4}, 2.51 \times 10^{-4}, 3.98 \times 10^{-4}, 6.31 \times 10^{-4}, 1.00 \times 10^{-3}, 1.58 \times 10^{-3}, 2.24 \times 10^{-3}, 3.31 \times 10^{-3}, 5.01 \times 10^{-3}, 7.08 \times 10^{-3}, 1.00 \times 10^{-2}\}$ Hz. The energy ranges used by A. C. Fabian et al. (2009) and A. Zoghbi et al. (2010) for their time lag calculations are 0.3–1 keV for the soft band and 1–4 keV for the hard band, as discussed in Paper I. We perform model fitting by varying the free parameters and comparing the resulting time lags with the data. The mass of the central black hole is set using $M = 4.90 \times 10^6 M_\odot$, which is in the range suggested by B. De Marco et al. (2013) and C. Done & C. Jin (2016). Based on this mass value, we can use Equation (40) to compute the corresponding values of the dimensionless angular frequency, $\tilde{\omega} = 2\pi R_g\, \nu_{\rm F}/c$, obtaining $\tilde{\omega} = (151.67\ \ \mathrm{s})\, \nu_{\rm F}$. Based on the assumed mass value, we can use Equation (8) to calculate the spherical Eddington limit for the source, obtaining $L_{\rm E} = 6.16 \times 10^{44}\ \mathrm{erg\ s^{-1}}$. The reference bolometric luminosity for the source reported by C. Done & C. Jin (2016) is $L_{\rm bol} \sim 3 \times 10^{44}\ \mathrm{erg\ s^{-1}}$, and therefore the Eddington ratio for the source is $L_{\rm bol}/L_{\rm E} = 0.49$, which implies that the dimensionless accretion rate $\dot{m} = 0.49$ (see Equation (12)). We note that the value of $\dot{m}$ here is about half of the value of $\dot{m}_{\rm SB}$ used in Paper I for the source 1H 0707−495. The discrepancy is due to the definition for $\dot{m}$ established in Equation (14), which includes the bolometric efficiency factor, $\eta_{\rm bol}$. This factor was not included in the definition of $\dot{m}_{\rm SB}$ adopted in Paper I.

Following the procedure discussed in Sections 2 and 3, for each Fourier frequency, we compute the first 21 eigenvalues λ_n and the corresponding sets of eigenfunctions $\mathcal{G}_n$ and $\mathcal{H}_n$. The real and imaginary parts of the complex eigenvalues are plotted in Figure 2. The theoretical time lags are then computed for each observational angular frequency ω using Equation (78), and plotted in Figure 3 (solid green line), along with the observational time lag data reported by A. C. Fabian et al. (2009) and A. Zoghbi et al. (2010). Figure 3 also includes

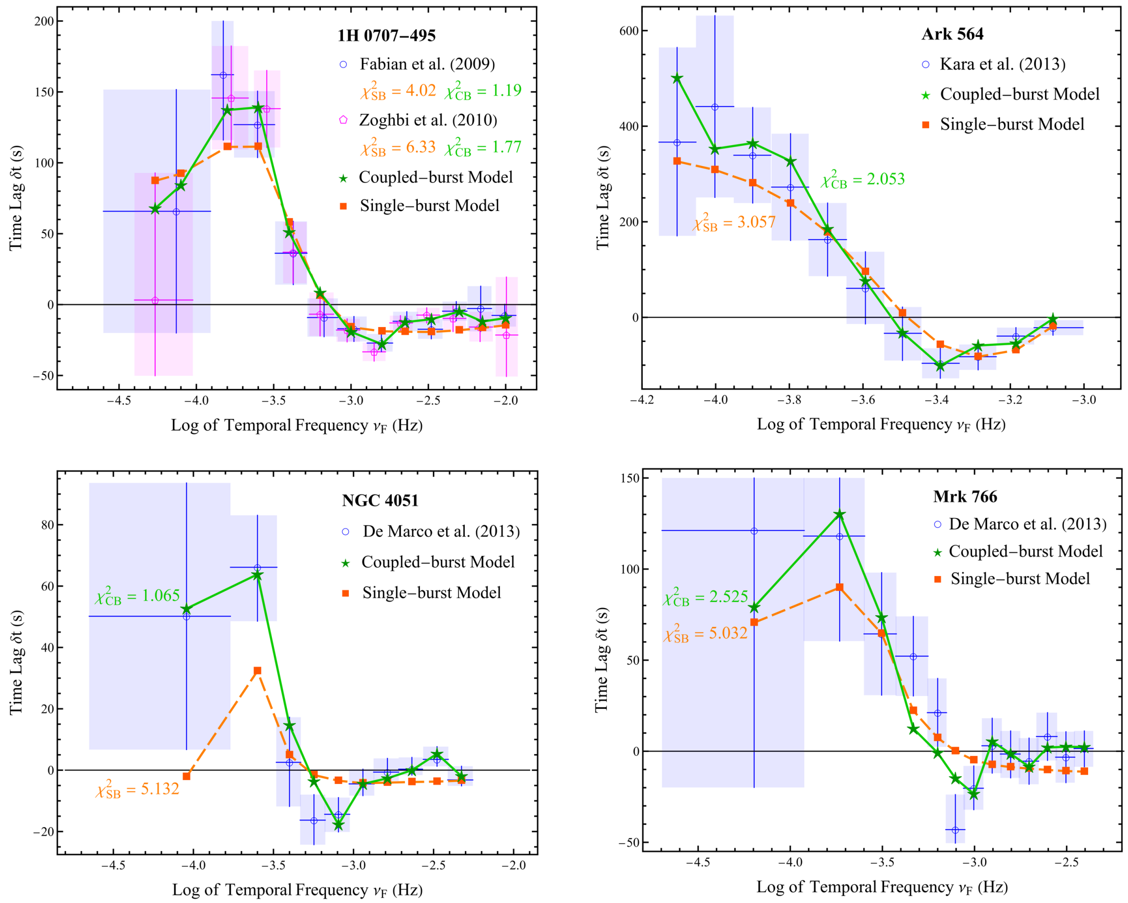

Figure 3. Plots of the time lag as a function of Fourier frequency for 1H 0707−495 (top left), Ark 564 (top right), NGC 4051 (bottom left), and Mrk 766 (bottom right). The observed time lags are indicated by open circles, with blue shaded regions indicating the error ranges. In the case of 1H 0707−495, two observational datasets are plotted, resulting in two sets of markers and error regions shown in blue and magenta. The solid green lines with star markers are the theoretical time lags computed using the coupled-burst model, and the dashed orange lines with square markers correspond to the single-burst model, as discussed in Paper I. The reduced chi-square values for the coupled-burst and single-burst model predictions are indicated by $\chi^2_{\rm CB}$ and $\chi^2_{\rm SB}$, respectively.

Table 2
Coupled-burst Model Auxiliary Parameter Values

Object	M ($10^6 M_\odot$)	$\dot{m}$	$\Delta q_{\rm prop}$	$\Delta t_{\rm prop}$ (hr)	ϵ_s (keV)	ϵ_h (keV)
1H 0707−495	4.90	0.487	3312.8	22.2	0.30	2.14
Ark 564	5.22	0.547	2310.0	16.5	0.46	2.53
NGC 4051	5.21	0.054	3280.3	23.4	0.30	2.32
Mrk 766	3.56	0.224	4772.1	23.2	0.30	2.17

the time lags computed using the single-burst model (dashed orange line; see Paper I). Due to the complexity of the calculations involved in the coupled-burst model, the fitting of the theoretical model to the data is performed via manual variation of the nine model free parameters, rather than using an automated process. However, we can nonetheless quantify the fit to the data by computing the reduced chi-square value, based on the fact that there are nine free parameters in our coupled-burst model. The details for this procedure are discussed in Section 4.5. In the application to 1H 0707−495, we obtain for the coupled-burst model $\chi^2_{\rm CB} = 1.190$ using the data from A. C. Fabian et al. (2009) and $\chi^2_{\rm CB} = 1.769$ using the A. Zoghbi et al. (2010) dataset. These are much better fits than those obtained using the single-burst model (also with nine free parameters), for which we find that $\chi^2_{\rm SB} = 4.024$ using the A. C. Fabian et al. (2009) data and $\chi^2_{\rm SB} = 6.335$ using the A. Zoghbi et al. (2010) data (see Figure 3).

The values obtained for the nine model free parameters in the application of the coupled-burst model to 1H 0707−495 are listed in Table 1, and the associated auxiliary parameters, which are either dependent on the free parameters, or directly constrained by the observational energy windows for the soft and hard energy bands, are likewise listed in Table 2. We summarize the results here. The outer radius of the hot, wedge-shaped inner region of the accretion disk is truncated at radius $r_{\rm out}$, which is a free parameter in our model. In the application to 1H 0707−495, we find that $r_{\rm out} = 100\,R_g$, which is the location of the standing shock wave. The inner radius is set to $r_{\rm in} = 1.61\,R_g$, which is the standard result for the inner radius of an accretion disk around a Kerr black hole with $a = 0.98$ (see Section 3.2). The value of the inclination angle between the black hole spin and the line of sight to an observer on Earth (a free parameter) suggested by our coupled-burst model is $\theta = 48°$, which agrees well with the relativistic reverberation model prediction $44° \leqslant \theta \leqslant 55°$ (A. Zoghbi et al. 2010). The opening angle of the wedge-shaped region (also a free parameter) is found to be $\Psi = 59°$, which indicates that the slope of the wedge region is $\hat{b} = 0.6$ (see Equation (18)). The bolometric efficiency, $\eta_{\rm bol}$, is a free parameter in our model, and in the application to 1H 0707−495, we find that

$\eta_{\rm bol} = 0.44$. This is a surprisingly high value for the bolometric efficiency, but it is within the acceptable range. Furthermore, we point out that the X-ray efficiency, $\eta_{\rm x}$, is significantly lower, since $\eta_{\rm x} = \eta_{\rm bol}/\kappa_{\rm bol}$ according to Equation (16), and $\kappa_{\rm bol}$ falls in the range $2 \lesssim \kappa_{\rm bol} \lesssim 20$ (V. Singh et al. 2011). The resulting X-ray efficiency is therefore in the range $0.022 \lesssim \eta_{\rm x} \lesssim 0.22$, which agrees with typical estimates.

The inner and outer burst radii, r_1 and r_2, respectively, are treated as free parameters in our coupled-burst model. In the case of 1H 0707−495, we find that the first burst of iron K and L photons occurs at radius $r_1 = 38\,R_g$. Subsequently, a pressure wave propagates outward and induces a second burst of iron K and L photons at radius $r_2 = 98\,R_g$, very close to the location of the standing shock, as discussed in Section 2.1. The Mach number $\mathscr{M}$ is a free parameter in our model, and we find that $\mathscr{M} = 0.705$ in the case of 1H 0707−495. This implies that the propagation time between the two bursts, computed using Equation (71), is $\Delta t_{\rm prop} = 22.2$ hr, and it follows that the corresponding dimensionless propagation time, measured in units of the light-crossing time for the gravitational radius, is given by $\Delta q_{\rm prop} = 3.31 \times 10^3\,R_g/c$. The relative strength of the second burst is represented by the ratio $N_{\rm K2}/N_{\rm K1}$, which is also a free parameter in our model. We find that in the application to 1H 0707−405, $N_{\rm K2}/N_{\rm K1} = 1.59$, which implies that the second burst releases 59% more iron K photons than the first burst. This indicates that 61% of the energy from the original thermal instability occurring at the inner source radius r_1 is dissipated in the vicinity of the standing shock, located close to the outer source radius r_2.

Similar to the single-burst model in Paper I, the coupled-burst model adopts precise values for the soft and hard X-ray light-curve energies, rather than using the observational windows, which have a finite width. Hence, in our model, the soft and hard channel energies, ϵ_s and ϵ_h, respectively, are considered to be auxiliary parameters. In the case of 1H 0707 −495, these parameters are constrained to fall within the energy windows $0.3 \leqslant \epsilon_s \leqslant 1$ keV and $1 \leqslant \epsilon_h \leqslant 4$ keV, which are specified in the observational time lag data reported by A. C. Fabian et al. (2009). The values we adopt for the soft and hard X-ray channel energies are $\epsilon_s = 0.30$ keV and $\epsilon_h = 2.14$ keV, respectively. The electron temperature of the wedge-shaped accretion region, T_e, is the final free parameter in our model, and in the case of 1H 0707−495, we find that $T_e = 1.01 \times 10^8$ K, or $k_{\rm B} T_e = 8.69$ keV, which is sufficiently hot to generate the emission of fluorescent iron K photons with energy $\epsilon_{\rm K} = 6.4$ keV.

4.2. Ark 564

The second source considered in our study is Ark 564, which is the brightest NLS1 galaxy in the X-rays and produces distinct X-ray time lags. This source was analyzed by I. E. Papadakis et al. (2007), who found that the low, hard state spectrum of Ark 564 exhibits a soft excess in the energy range 0.3–2 keV and an iron emission feature at energy 6.4–7.0 keV. They fitted the 0.3–11 keV spectrum of Ark 564 using the power-law, disk reflection, and additional line (`pl+dl+adl`) models in XSPEC, which together simulate the photoluminescence process, including delocalized electronic states and absorber-binding-luminescent localized states. However, they found that the resulting spectral fit was not acceptable unless they also included a component representing iron absorption in a warm medium at X-ray energy ∼8 keV. This suggests that the formation of the steady-state X-ray spectrum in Ark 564 is the result of a complex combination of physical effects.

For this source, our analysis is based on the set of observational time lags and associated Fourier frequencies presented by E. Kara et al. (2013b), corresponding to the energy range 0.3−1 keV for the soft band and 1.2−4 keV for the hard band. The mass of the central black hole is set using $M = 5.22 \times 10^6 M_\odot$, which agrees with the range suggested by B. De Marco et al. (2013), $0.59 \times 10^6 M_\odot \leqslant M \leqslant 5.88 \times 10^6 M_\odot$. The set of theoretical Fourier frequencies we use in our analysis for this source corresponds to the observational values reported by E. Kara et al. (2013b), given by $\nu_{\rm F} \in \{7.86 \times 10^{-5}$, 9.95×10^{-5}, 1.26×10^{-4}, 1.60×10^{-4}, 2.01×10^{-4}, 2.55×10^{-4}, 3.22×10^{-4}, 4.07×10^{-4}, 5.15×10^{-4}, 6.53×10^{-4}, $8.24 \times 10^{-3}\}$ Hz. Based on Equation (40), we find that the dimensionless Fourier frequency, $\tilde{\omega}$, is related to the observational Fourier frequency, $\nu_{\rm F}$, via $\tilde{\omega} = (161.57\ \ {\rm s})\,\nu_{\rm F}$. Based on the adopted mass value, the Eddington luminosity calculated using Equation (8) is $L_{\rm E} = 6.56 \times 10^{44}$ erg s^{-1}. The X-ray luminosity of Ark 564 in the 2–10 keV energy range found by E. Kara et al. (2017) is $L_{\rm X} = 3.9 \times 10^{43}$ erg s^{-1}, based on the best-fitting `xillmodel` model. The bolometric correction they used is $\kappa_{\rm bol} = 9.2 \pm 4.5$, taken from R. V. Vasudevan & A. C. Fabian (2007), which gives the bolometric luminosity $L_{\rm bol} = 3.59 \times 10^{44}$ erg s^{-1}. According to Equation (12), we therefore find that $\dot{m} = L_{\rm bol}/L_{\rm E} = 0.547$ falls between the low value, $L_{\rm bol}/L_{\rm E} = 0.204$, estimated by V. Singh et al. (2011), and the high value, $L_{\rm bol}/L_{\rm E} = 1.1$, estimated by E. Kara et al. (2017), for this source. The value of $\dot{m}$ adopted here is about half of the value of $\dot{m}_{\rm SB}$ used in Paper I for the source Ark 564, which is due to the definition for $\dot{m}$ given in Equation (14), where the bolometric efficiency factor $\eta_{\rm bol}$ is included. This factor was not included in the definition of $\dot{m}_{\rm SB}$ adopted in Paper I.

The model free parameters are varied in order to obtain an acceptable qualitative fit to the time lag data taken from E. Kara et al. (2013b). The resulting values for the nine model free parameters are listed in Table 1, and the associated auxiliary parameters are listed in Table 2. Following the steps discussed in Sections 2 and 3, we determine the first 22 eigenvalues λ_n and the corresponding eigenfunctions $\mathcal{G}_n$ and $\mathcal{H}_n$ for each Fourier frequency. The set of complex eigenvalues we obtain for this source is plotted in Figure 2. Based on these results, we calculate the theoretical time lags for Ark 564 using the coupled-burst model developed here. We vary the values of the free parameters to find the best qualitative fit between the theoretical time lags and the observational time lag data. The theoretical time lags are plotted in Figure 3 (solid green line), along with the observational time lags reported by E. Kara et al. (2013b), and the time lags computed using the single-burst model developed in Paper I (dashed orange line). Using the procedure described in Section 4.5, we find that the fit to the data obtained using the coupled-burst model yields the reduced chi-square value $\chi^2_{\rm CB} = 2.053$, indicating a slightly better fit than that obtained using the single-burst model, which yields $\chi^2_{\rm SB} = 3.057$.

The best qualitative fit to the observational time lag data obtained using the coupled-burst model results from the following values for the nine model free parameters (see also Table 1). The outer radius of the wedge-shaped inner region is found to be $r_{\rm out} = 100\,R_g$, and the inner radius is fixed at $r_{\rm in} = 1.61\,R_g$ as in the other cases. We find that the inclination angle between the spin axis of the disk and the line of sight to Earth is $\theta = 36°$, which is consistent with the range $27.^{\circ}21 \leqslant \theta \leqslant 38.^{\circ}03$ reported by S. Barua et al. (2020) for this source. The opening angle of the wedge-shaped region is found to be $\Psi = 55°$, which is equivalent to the slope parameter value $\hat{b} = 0.7$, according to Equation (18). The bolometric efficiency for Ark 564 obtained using our coupled-burst model is $\eta_{\rm bol} = 0.498$, which implies that the associated X-ray efficiency is $\eta_{\rm X} = 0.054$ according to the bolometric correction value $\kappa_{\rm bol} = 9.2$ and Equation (16).

Our coupled-burst model also treats the inner and outer burst radii, r_1 and r_2, and the Mach number, $\mathscr{M}$, as free parameters. For Ark 564, we obtain $r_1 = 42\,R_g$, $r_2 = 86\,R_g$, and $\mathscr{M} = 0.717$. The propagation time delay between the first and second bursts of iron K and L photons, computed using Equation (71), is $\Delta t_{\rm prop} = 16.5$ hr, or $\Delta q_{\rm prop} = 2.31 \times 10^3\,R_g/c$ (see also Table 2). For this source, we find that $N_{\rm K2}/N_{\rm K1} = 3.03$, indicating that 75% of the energy from the thermal instability is dissipated in the second burst of iron K photons located at radius r_2 near the location of the standing shock at the outer boundary of the wedge-shaped inner region. The specific values adopted for the soft and hard X-ray channel energies are $\epsilon_s = 0.46$ keV and $\epsilon_h = 2.53$ keV, respectively. These values are consistent with the energy windows reported by E. Kara et al. (2013b). The last free parameter in our coupled-burst model is the electron temperature, T_e, which has the value $T_e = 2.19 \times 10^8$ K, or $k_{\rm B} T_e = 18.91$ keV, in our application to Ark 564. This is sufficiently hot to generate fluorescent iron K photons, and it is in rough agreement with the temperature value obtained using the spectral analysis reported by E. Kara et al. (2017).

4.3. NGC 4051

Another source we consider is NGC 4051, an intermediate spiral galaxy discovered in 1788 by William Herschel. It is identified as an NLS1 galaxy with rapid X-ray variability (F. E. Marshall et al. 1983; M. Guainazzi et al. 1998; Y. Terashima et al. 2009). The X-ray spectrum of NGC 4051 has a complex shape that is challenging to model. This has resulted in the utilization of sophisticated combinations of emission and absorption components in XSPEC. For example, E. Seifina et al. (2018) studied the low, hard state spectrum of NGC 4051 using a model comprising blackbody radiation combined with absorption, computed using the `gabs` model, along with the `bmc` model, which simulates the effect of bulk-motion Comptonization (L. Titarchuk & E. Seifina 2017). They also included recombination edge emission and a Laor iron emission line at 6.4 keV. Although the spectral fit they obtained is acceptable, the complexity of the model tends to obscure the detailed nature of the underlying physical processes occurring in the various regions of the accretion disk surrounding the central black hole.

We analyze the time lag data for NGC 4051 presented by B. De Marco et al. (2013), who computed time lags for the set of Fourier frequencies $\nu_{\rm F} \in \{9.05 \times 10^{-5}$,o 2.51×10^{-4}, 3.98×10^{-4}, 5.66×10^{-4}, 8.05×10^{-4}, 1.15×10^{-3}, 1.63×10^{-3}, 2.32×10^{-3}, 3.32×10^{-3}, $4.73 \times 10^{-3}\}$ Hz. We adopt the same Fourier frequency values for our theoretical analysis. The energy ranges used by B. De Marco et al. (2013) for this source are 0.3–1 keV for the soft band and 1–5 keV for the hard band. Additional time lag observations for this source were discussed by L. Miller et al. (2010b). The value of the black hole mass assumed is $M = 5.21 \times 10^6 M_{\odot}$, which is above the lower limit reported by E. Seifina et al. (2018), and in rough agreement with the estimates presented by K. D. Denney et al. (2009) and B. M. Peterson et al. (2004). The mass value we use is significantly higher than that estimated using reverberation mapping by M. C. Bentz & S. Katz (2015), although we note that the reverberation method is itself model dependent, and involves making assumptions about the mass scale (or virial) factor required to relate the statistics for AGNs with those of quiescent galaxies. The dimensionless Fourier frequency calculated using Equation (40), along with the assumed value for the black hole mass, is $\tilde{\omega} = (161.37\quad {\rm s})\,\nu_{\rm F}$, which can be combined with the Fourier frequencies from B. De Marco et al. (2013) to obtain $\tilde{\omega} \in \{1.46 \times 10^{-2}, 4.05 \times 10^{-2}, 6.42 \times 10^{-2}, 9.14 \times 10^{-2}, 1.30 \times 10^{-1}, 1.85 \times 10^{-1}, 2.63 \times 10^{-1}, 3.74 \times 10^{-1}, 5.36 \times 10^{-1}, 7.63 \times 10^{-1}\}$.

Based on the XMM observations reported by K. A. Pounds et al. (2004), we set the X-ray luminosity value using $L_{\rm X} = 7 \times 10^{41}$ erg s^{-1}. In order to estimate the bolometric luminosity, we adopt the value $\kappa_{\rm bol} = 50.12$, taken from F. Duras et al. (2020), which yields $L_{\rm bol} = 3.51 \times 10^{43}$ erg s^{-1}. Using the adopted black hole mass, $M = 5.21 \times 10^6 M_{\odot}$, we find that the Eddington luminosity is given by $L_{\rm E} = 6.55 \times 10^{44}$ erg s^{-1}. We therefore set the dimensionless mass accretion rate to $\dot{m} = L_{\rm bol}/L_{\rm E} = 0.054$ (see Equation (12)).

For each value of $\tilde{\omega}$, we follow the procedure discussed in Sections 2 and 3 to compute the first 27 eigenvalues λ_n and the corresponding eigenfunctions $\mathcal{G}_n$ and $\mathcal{H}_n$. The first 20 eigenvalues are plotted in the complex plane in Figure 2. The optimal theoretical time lags are plotted in Figure 3 (the green solid line), along with the time lag data reported B. De Marco et al. (2013), and the theoretical time lags computed using the single-burst model (dashed orange line). It is interesting to analyze the quality of the fit by computing the reduced chi-square statistic using the procedure developed in Section 4.5. The optimal theoretical time lags obtained using the coupled-burst model agree fairly well with the observational data, with a reduced chi-square value $\chi^2_{\rm CB} = 1.065$. This agreement is nearly 5 times better than that obtained using the single-burst model, with $\chi^2_{\rm SB} = 5.132$.

We vary the nine model free parameters to obtain an optimal fit to the observational time lag distribution for NGC 4051 reported by B. De Marco et al. (2013). The resulting free parameter values are listed in Table 1, and the associated auxiliary parameter values are provided in Table 2. We find that the outer boundary of the wedge-shaped region is located at radius $r_{\rm out} = 120\,R_g$, while the inner radius of the wedge-shaped region is fixed at $r_{\rm in} = 1.61\,R_g$ (see Section 3.2). The inclination angle of NGC 4051 implied by our coupled-burst model is $\theta = 22°$, and the opening angle of the wedge-shaped accretion region is $\Psi = 55°$, indicating that the value of the slope parameter is $\hat{b} = 0.7$. The bolometric efficiency is found to be $\eta_{\rm bol} = 0.059$, which is a relatively low efficiency, but nonetheless within the expected range for an accreting supermassive black hole. Using Equation (16), along with the bolometric correction value $\kappa_{\rm bol} = 50.12$, we can compute the X-ray efficiency, $\eta_{\rm X}$, obtaining $\eta_{\rm X} = 0.0012$.

The values of the inner and outer burst radii suggested by our coupled-burst model are $r_1 = 44\,R_g$ and $r_2 = 100\,R_g$, respectively, and the Mach number of the postshock accretion flow is found to be $\mathscr{M} = 0.704$. The propagation time between the two bursts can therefore be calculated using Equation (71), yielding $\Delta t_{\rm prop} = 23.4$ hr, or $\Delta q_{\rm prop} = 3.28 \times 10^3\, R_g/c$. We also find that the second burst produces 5.00 times more iron K photons than the first burst, so that $N_{\rm K2}/N_{\rm K1} = 5.00$, which indicates that 83% of the energy injected by the thermal instability is dissipated in the second burst of seed photons, which occurs near the standing shock located at the outer edge of the hot, wedge-shaped region. In our model fitting, we utilize the values $\epsilon_s = 0.30$ keV and $\epsilon_h = 2.32$ keV, which are compatible with the channel energy values reported by B. De Marco et al. (2013). The value of the electron temperature, which is our final free parameter, is $T_e = 2.43 \times 10^8$ K, or $k_{\rm B} T_e = 20.95$ keV, which is sufficient to generate fluorescent iron K emission.

4.4. Mrk 766

The last source discussed in this study is Mrk 766 (also known as NGC 4253), which is an NLS1 galaxy that displays strong Fe II emission (D. J. K. Buisson et al. 2018). The steady-state X-ray spectrum of Mrk 766 was analyzed by S. Giacchè et al. (2014) using the XSPEC models `bmc` (bulk-motion Comptonization), `pexrav` (reflected power-law emission), and `zxipcf`, which is a redshifted partial covering model with ionized material. They found that the resulting theoretical spectrum is dominated by a low-energy blackbody component with temperature $k_{\rm B} T_e \sim 0.1$ keV combined with absorption and an iron emission feature at energy $\sim$6$-$8 keV. Hence, once again we conclude that the steady-state X-ray spectrum for this source is the result of a complex set of physical processes.

Based on the time lag data for this source reported by B. De Marco et al. (2013), the set of Fourier frequencies we use in our calculation of the theoretical time lags is $\nu_{\rm F} \in \{6.37 \times 10^{-5}, 1.85 \times 10^{-4}, 3.13 \times 10^{-4}, 4.66 \times 10^{-4}, 6.31 \times 10^{-4}, 7.87 \times 10^{-4}, 9.91 \times 10^{-4}, 1.25 \times 10^{-3}, 1.57 \times 10^{-3}, 1.98 \times 10^{-3}, 2.49 \times 10^{-3}, 3.13 \times 10^{-3}, 3.94 \times 10^{-3}\}$ Hz. The energy ranges used by B. De Marco et al. (2013) when computing the time lags for Mrk 766 are 0.3$-$0.7 keV for the soft band and 1.5$-$4 keV for the hard band. We set the black hole mass using $M = 3.56 \times 10^6 M_\odot$, which lies between the estimates reported by M. C. Bentz et al. (2009), D. J. K. Buisson et al. (2018), and K. Oh et al. (2025). Substituting this value into Equation (40), we can compute the dimensionless Fourier frequencies using $\tilde{\omega} = (110.09\quad {\rm s})\, \nu_{\rm F}$, which yields $\tilde{\omega} \in \{7.01 \times 10^{-3}, 2.04 \times 10^{-2}, 3.45 \times 10^{-2}, 5.13 \times 10^{-2}, 6.95 \times 10^{-2}, 8.66 \times 10^{-2}, 1.09 \times 10^{-1}, 1.37 \times 10^{-1}, 1.73 \times 10^{-1}, 2.18 \times 10^{-1}, 2.74 \times 10^{-1}, 3.45 \times 10^{-1}, 4.34 \times 10^{-1}\}$. Based on Equation (8) and the adopted value of the black hole mass, we find that the Eddington luminosity is given by $L_{\rm E} = 4.47 \times 10^{44}$ erg s^{-1}. Combining this with the bolometric luminosity reported by R. V. Vasudevan et al. (2010), M. J. Koss et al. (2022), and K. Oh et al. (2025), $L_{\rm bol} \sim 1 \times 10^{44}$, we find that the dimensionless accretion ratio is $\dot{m} = L_{\rm bol}/L_{\rm E} = 0.22$ (see Equation (12)).

We determine the first 21 eigenvalues λ_n, the first 20 of which are plotted in Figure 2, and compute the corresponding sets of eigenfunctions $\mathcal{G}_n$ and $\mathcal{H}_n$. The optimal results for the theoretical time lags obtained using the coupled-burst model are plotted in Figure 3 (solid green line), which also includes a comparison with the optimal single-burst model time lags (dashed orange line), and the observational time lags reported by B. De Marco et al. (2013). Next we compute the reduced chi-square statistic using the procedure discussed in Section 4.5. We find that the time lag distribution obtained using the coupled-burst model, with reduced chi-square value $\chi^2_{\rm CB} = 2.525$, fits the observational data significantly better than the single-burst model, with $\chi^2_{\rm SB} = 5.032$ (see Figure 3).

The associated values of the nine free parameters used to produce the optimal fit to the time lag data for Mrk 766 based on the coupled-burst model are listed in Table 1, and the associated auxiliary parameters are listed in Table 2. In the case of Mrk 766, we find that the outer radius of the wedge-shaped region is located at $r_{\rm out} = 120\, R_g$ while we fix the inner radius at $r_{\rm in} = 1.61\, R_g$. The inclination angle of Mrk 766 obtained is $\theta = 40°$, which agrees with the model prediction reported by D. J. K. Buisson et al. (2018). The wedge opening angle is found to be $\Psi = 59°$, which indicates that the value of the slope parameter for the wedge-shaped region is $\hat{b} = 0.6$ according to Equation (18). We find that the bolometric efficiency is equal to $\eta_{\rm bol} = 0.249$, which suggests that the X-ray efficiency is $\eta_{\rm x} = 0.031$, where we have utilized the bolometric correction $\kappa_{\rm bol} = 7.9$, as suggested by R. V. Vasudevan et al. (2010).

The first and second bursts of iron K and L seed photons, treated as free parameters, are found to occur at radii $r_1 = 26\, R_g$ and $r_2 = 114\, R_g$, respectively. The Mach number is a free parameter, and we find that $\mathscr{M} = 0.742$ in the application to Mrk 766. It therefore follows from Equation (71) that the propagation time from the first to the second burst is $\Delta t_{\rm prop} = 23.2$ hr, or $\Delta q_{\rm prop} = 4.77 \times 10^3\, R_g/c$. We find that the relative strength of the second burst for Mrk 766 is $N_{\rm K2}/N_{\rm K1} = 2.38$, suggesting that 70% of the energy from the thermal instability is dissipated at the standing shock, which is located near the outer source radius, r_2. In our analysis of Mrk 766, we set the soft X-ray channel energy using $\epsilon_s = 0.30$ keV and the hard channel energy using $\epsilon_h = 2.17$ keV, which are consistent with the analysis carried out by B. De Marco et al. (2013). The value we obtain for the electron temperature in the wedge-shaped region, which is also a free parameter, is $T_e = 1.19 \times 10^8$ K, or $k_{\rm B} T_e = 10.22$ keV. This is sufficiently hot to generate the fluorescent iron K seed photons.

4.5. Error Analysis

In order to evaluate the accuracy of the theoretical models, we calculate the reduced chi-square value based on the statistical relation between the observational and theoretical data, given by

$$\chi^2_{\rm red} = \frac{1}{\tt dof} \sum_{n=1}^{N_{\rm data}} \frac{({\tt D}_n - {\tt T}_n)^2}{\sigma_n^2}, \tag{81}$$

where ${\tt dof} = N_{\rm data} - N_{\rm free}$ is the number of degrees of freedom, $N_{\rm data}$ denotes the number of data points, $N_{\rm free}$ represents the number of free parameters varied in the model, σ_n denotes the standard deviation for each point in the dataset, and ${\tt D}_n$ and ${\tt T}_n$ denote the observational data and theoretical values associated with the nth frequency value, respectively. The value of σ_n is set equal to half of the total error range in the observational time lag data, and therefore this quantity varies with the observational Fourier frequency for each source. The nine free parameters used in the coupled-burst model are listed in Table 1, and therefore

Table 3
Statistical Parameters

Object	$N_{\rm data}$	$N_{\rm free}$	dof	$\chi^2_{\rm SB}$	$\chi^2_{\rm CB}$	Citation
1H 0707−495	12	9	3	4.024	1.190	A. C. Fabian et al. (2009)
1H 0707−495	12	9	3	6.335	1.769	A. Zoghbi et al. (2010)
Ark 564	11	9	2	3.057	2.053	E. Kara et al. (2013b)
NGC 4051	10	9	1	5.132	1.065	B. De Marco et al. (2013)
Mrk 766	13	9	4	5.032	2.525	B. De Marco et al. (2013)

Table 4
1H 0707−495 Errors from A. C. Fabian et al. (2009)

Single-burst Model				Coupled-burst Model			
n	$(\mathtt{D}_n - \mathtt{T}_n)^2$	σ_n^2	$\frac{(\mathtt{D}_n - \mathtt{T}_n)^2}{\sigma_n^2}$	n	$(\mathtt{D}_n - \mathtt{T}_n)^2$	σ_n^2	$\frac{(\mathtt{D}_n - \mathtt{T}_n)^2}{\sigma_n^2}$
1	654.567	7367.15	8.885×10^{-2}	1	238.068	7367.15	3.231×10^{-2}
2	2762.55	1762.24	1.568×10^{0}	2	871.51	1762.24	4.945×10^{-1}
3	241.772	548.768	4.406×10^{-1}	3	147.866	548.768	2.695×10^{-1}
4	222.975	497.350	4.483×10^{-1}	4	84.1838	497.350	1.693×10^{-1}
5	158.378	182.068	8.699×10^{-1}	5	193.634	182.068	1.064×10^{0}
6	0.694321	77.5826	8.949×10^{-3}	6	9.20157	77.5826	1.186×10^{-1}
7	70.0116	38.2469	1.831×10^{0}	7	0.385552	38.2469	1.008×10^{-2}
8	54.5473	48.0808	1.134×10^{0}	8	0.240581	48.0808	5.004×10^{-3}
9	3.73614	48.0808	7.771×10^{-2}	9	49.8689	48.0808	1.037×10^{0}
10	184.703	45.5170	4.058×10^{0}	10	0.689705	45.5170	1.515×10^{-2}
11	190.064	253.750	7.490×10^{-1}	11	74.5272	253.750	2.937×10^{-1}
12	49.537	61.9536	7.996×10^{-1}	12	3.78867	61.9537	6.115×10^{-2}

Table 5
1H 0707−495 Errors from A. Zoghbi et al. (2010)

Single-burst Model				Coupled-burst Model			
n	$(\mathtt{D}_n - \mathtt{T}_n)^2$	σ_n^2	$\frac{(\mathtt{D}_n - \mathtt{T}_n)^2}{\sigma_n^2}$	n	$(\mathtt{D}_n - \mathtt{T}_n)^2$	σ_n^2	$\frac{(\mathtt{D}_n - \mathtt{T}_n)^2}{\sigma_n^2}$
1	7064.33	5114.69	1.381×10^{0}	1	4171.02	5114.69	8.155×10^{-1}
2	1185.85	1328.97	8.923×10^{-1}	2	67.6299	1328.97	5.089×10^{-2}
3	1725.97	738.056	2.339×10^{0}	3	546.083	738.056	7.399×10^{-1}
4	212.001	466.319	4.546×10^{-1}	4	76.4747	466.319	1.640×10^{-1}
5	171.716	234.858	7.311×10^{-1}	5	228.838	234.858	9.744×10^{-1}
6	23.7252	66.0471	3.592×10^{-1}	6	4.96517	66.0471	7.518×10^{-2}
7	232.420	42.2631	5.499×10^{0}	7	57.8967	42.2632	1.370×10^{0}
8	37.7061	26.0953	1.445×10^{0}	8	6.79600	26.0953	2.604×10^{-1}
9	141.326	28.5216	4.955×10^{0}	9	10.7754	28.5216	3.778×10^{-1}
10	74.1617	82.0062	9.043×10^{-1}	10	13.4410	82.0062	1.639×10^{-1}
11	0.580738	109.180	5.319×10^{-3}	11	21.4502	109.180	1.965×10^{-1}
12	47.6753	1229.34	3.878×10^{-2}	12	145.016	1229.34	1.180×10^{-1}

$N_{\rm free} = 9$. This is also equal to the number of model free parameters used in the single-burst model from Paper I. The values of $\chi^2_{\rm red}$ computed using Equation (81) based on either the single-burst model or the coupled-burst model are referred to as the $\chi^2_{\rm SB}$ or $\chi^2_{\rm CB}$, respectively. In Table 3, we list the values for $\chi^2_{\rm SB}$ and $\chi^2_{\rm CB}$ computed using Equation (81) for each of the sources treated here, along with the corresponding number of data points, $N_{\rm data}$, the number of free parameters, $N_{\rm free}$, and the number of degrees of freedom, dof. These results are discussed in detail for each individual source below. In most cases, $\mathtt{D}_n - \mathtt{T}_n$ is simply equal to the mean observational time lag minus the theoretical time lag evaluated at each Fourier frequency in the observational dataset. An exception is the case of 1H 0707−495, where a single theoretical model (either single-burst or coupled-burst) is used to analyze simultaneously the combined time lag data taken from both A. C. Fabian et al. (2009) and A. Zoghbi et al. (2010). In this case, we evaluate the theoretical time lags at the observational Fourier frequencies using linear interpolation from the set of frequencies used in the theoretical analysis. The individual contributions to the error sum in Equation (81) made by each observational time lag data point for each of the four sources treated here are listed in Tables 4–8 for both the single-burst and coupled-burst models. We note that the summary of chi-square results presented in Table 3 can be reproduced by adding the values

Table 6
Ark 564 Errors from E. Kara et al. (2013b)

Single-burst Model				Coupled-burst Model			
n	$(\mathrm{D}_n - \mathrm{T}_n)^2$	σ_n^2	$\frac{(\mathrm{D}_n - \mathrm{T}_n)^2}{\sigma_n^2}$	n	$(\mathrm{D}_n - \mathrm{T}_n)^2$	σ_n^2	$\frac{(\mathrm{D}_n - \mathrm{T}_n)^2}{\sigma_n^2}$
1	1633.29	38,832.2	4.206×10^{-2}	1	18,133.4	38,832.2	4.670×10^{-1}
2	17,587.2	36,174.5	4.862×10^{-1}	2	7835.72	36,174.5	2.166×10^{-1}
3	3405.38	10,000.0	3.405×10^{-1}	3	648.240	10,000.0	6.482×10^{-2}
4	1166.82	12,491.3	9.341×10^{-2}	4	2983.55	12,491.3	2.388×10^{-1}
5	220.145	5847.75	3.765×10^{-2}	5	494.133	5847.75	8.450×10^{-2}
6	1195.87	5698.77	2.098×10^{-1}	6	234.744	5698.77	4.119×10^{-2}
7	1758.07	3122.84	5.630×10^{-1}	7	1.86372	3122.84	5.968×10^{-4}
8	1512.29	984.237	1.537×10^{0}	8	23.245	984.237	2.362×10^{-2}
9	0.00618139	700.692	8.822×10^{-6}	9	551.673	700.692	7.873×10^{-1}
10	862.318	311.419	2.769×10^{0}	10	234.316	311.419	7.524×10^{-1}
11	8.77947	246.059	3.568×10^{-2}	11	351.658	246.059	1.429×10^{0}

Table 7
NGC 4051 Errors from B. De Marco et al. (2013)

Single-burst Model				Coupled-burst Model			
n	$(\mathrm{D}_n - \mathrm{T}_n)^2$	σ_n^2	$\frac{(\mathrm{D}_n - \mathrm{T}_n)^2}{\sigma_n^2}$	n	$(\mathrm{D}_n - \mathrm{T}_n)^2$	σ_n^2	$\frac{(\mathrm{D}_n - \mathrm{T}_n)^2}{\sigma_n^2}$
1	2738.22	7551.78	3.626×10^{-1}	1	6.25645	7551.78	8.285×10^{-4}
2	1143.92	1190.58	9.608×10^{-1}	2	5.34769	1190.58	4.492×10^{-3}
3	5.5764	845.267	6.597×10^{-3}	3	146.897	845.267	1.738×10^{-1}
4	216.231	265.492	8.145×10^{-1}	4	159.210	265.492	6.000×10^{-1}
5	119.571	125.040	9.563×10^{-1}	5	11.1705	125.040	8.934×10^{-2}
6	0.0501538	74.4113	6.740×10^{-4}	6	3.026×10^{-6}	74.4113	4.066×10^{-8}
7	11.7025	53.9967	2.167×10^{-1}	7	4.07581	53.9967	7.548×10^{-2}
8	17.4338	33.0717	5.272×10^{-1}	8	0.112018	33.0717	3.387×10^{-3}
9	52.4752	40.8292	1.285×10^{0}	9	3.33228	40.8292	8.162×10^{-2}
10	0.0501794	40.8292	1.229×10^{-3}	10	1.49901	40.8292	3.671×10^{-2}

Table 8
Mrk 766 Errors from B. De Marco et al. (2013)

Single-burst Model				Coupled-burst Model			
n	$(\mathrm{D}_n - \mathrm{T}_n)^2$	σ_n^2	$\frac{(\mathrm{D}_n - \mathrm{T}_n)^2}{\sigma_n^2}$	n	$(\mathrm{D}_n - \mathrm{T}_n)^2$	σ_n^2	$\frac{(\mathrm{D}_n - \mathrm{T}_n)^2}{\sigma_n^2}$
1	2559.77	7213.87	3.548×10^{-1}	1	1768.93	7213.87	2.452×10^{-1}
2	801.910	2003.44	4.003×10^{-1}	2	147.667	2003.44	7.371×10^{-2}
3	0.0482322	1130.60	4.266×10^{-5}	3	83.6259	1130.60	7.397×10^{-2}
4	897.860	476.726	1.883×10^{0}	4	1580.52	476.726	3.315×10^{0}
5	191.399	352.587	5.428×10^{-1}	5	486.424	352.587	1.380×10^{0}
6	1856.28	177.390	1.046×10^{1}	6	793.470	177.390	4.473×10^{0}
7	237.346	144.210	1.646×10^{0}	7	9.78653	144.210	6.786×10^{-2}
8	109.273	226.969	4.814×10^{-1}	8	5.64577	226.969	2.487×10^{-2}
9	51.5256	165.948	3.105×10^{-1}	9	0.0236652	165.948	1.426×10^{-4}
10	16.5542	160.371	1.032×10^{-1}	10	9.43723	160.371	5.885×10^{-2}
11	337.179	171.621	1.965×10^{0}	11	36.4065	171.621	2.121×10^{-1}
12	58.0824	195.267	2.975×10^{-1}	12	33.0704	195.267	1.694×10^{-1}
13	161.945	96.5371	1.678×10^{0}	13	0.597019	96.5371	6.184×10^{-3}

in the final numerical columns in Tables 4–8 and then dividing by the number of degrees of freedom for each source. In the case of 1H 0707−495, separate results are computed using the data from A. C. Fabian et al. (2009) and A. Zoghbi et al. (2010), with the individual error contributions listed in Tables 4 and 5, respectively.

5. Discussion and Conclusion

X-ray Fourier time lags, δt, observed from AGNs provide the clearest evidence for the existence of high-energy processes occurring on short timescales in the inner regions of the accretion disks around supermassive black holes. This is because Fourier time lags cannot be generated by a source with steady emission, and their presence therefore directly implies the presence of true secular variability in the underlying emission mechanism. Time lag observations for NLS1 sources are particularly challenging to explain due to the occurrence of both hard and soft X-ray time lags at different Fourier frequencies within the same observation. This has stimulated the development of a variety of theoretical models that tend to rely on complex geometrical scenarios, in which soft UV seed photons from the cool outer disk are upscattered in a hot corona, followed by downscattering of the resulting X-rays in the underlying inner region of the disk (e.g., J. Malzac & E. Jourdain 2000; L. Miller et al. 2010a; A. Zoghbi et al. 2010). In this paper, we have explored an alternative scenario in which the complex X-ray time lag behavior results from the injection of coupled sets of fluorescent iron K and L seed photons that are reprocessed via Compton reverberation in the accretion disk. We summarize the overall structure of the new model below.

5.1. Review of Main Results

We have developed a new physical model describing the Compton reverberation of seed photons taking place in the hot inner region of the accretion disk around the central black hole in an NLS1 galaxy. Here, the concept of Compton reverberation includes the thermal and bulk Comptonization of the seed photons, combined with particle injection and escape, and diffusive and advective transport. We show that the new model can explain the complex behavior observed in the Fourier time lags exhibited by NLS1 galaxies as a consequence of two coupled bursts of iron K and L seed photons that occur at inner and outer injection radii r_1 and r_2 and at injection times t_1 and t_2, respectively. The process begins with an impulsive flash of X-rays generated in the hot corona within a few gravitational radii from the event horizon due to the upscattering of soft photons produced in the cool outer region of the disk (M. Mizumoto et al. 2018; M. Szanecki et al. 2020; T. Boller et al. 2021). The flash of high-energy radiation is driven fundamentally by the acceleration of energetic electrons due to impulsive magnetic reconnection events occurring in the corona (J. Malzac & E. Jourdain 2000; P. Uttley et al. 2014). The strong gravitational deflection close to the black holes causes a large fraction of X-rays from the corona to be absorbed in the hot inner region of the accretion disk, which excites the local iron atoms (A. C. Fabian & S. Vaughan 2003; G. Miniutti & A. C. Fabian 2004; A. Zoghbi et al. 2010). The excited atoms radiatively decay, resulting in the emission of fluorescent iron K and L photons with energies $\epsilon_{\rm K}$ and $\epsilon_{\rm L}$, respectively, which are reprocessed via electron scattering in the disk plasma, eventually escaping to form the observed X-ray spectrum (A. Martocchia & G. Matt 1996; T. Boller et al. 2021). The flash of high-energy radiation from the corona also triggers a thermal instability that drives a pressure wave which propagates outward at the local sound speed (J. Hameury et al. 2009; D. Lawther et al. 2023). The energy in this wave is eventually dissipated at the location of the standing shock wave at the outer boundary of the hot inner region because the pressure wave cannot propagate into the supersonic region upstream from the shock. The dissipated energy generates a flash of bremsstrahlung radiation, which excites the iron atoms, resulting in another burst of fluorescent iron K and L seed photons at radius r_2 and time t_2. The outward propagation of the energy terminates at the standing shock wave, because the pressure wave cannot propagate outward into the supersonic upstream region.

In the case of the first burst occurring at radius r_1, the temperature is quite high, with $T_e \sim 10^8$ K, in which case detailed simulations show that K-shell photoionization results in the production of an iron K seed photon $\sim$30% of the time (M. O. Krause 1979; J. S. Kaastra & R. Mewe 1993), or otherwise results in the ejection of an Auger electron. Once the hole in the K shell is filled, the cascade proceeds with the filling of the hole in the L shell, which results in the ejection of an Auger electron 99.9% of the time, and therefore the emission of an iron L seed photon occurs with a probability of $\sim 10^{-3}$. These statistical results apply to the inner burst, and therefore we set $N_{\rm L1} = 10^{-3} N_{\rm K1}$. Conversely, for the outer burst, which occurs at radius r_2, the temperature is close to the value in the cooler UV-emitting, geometrically thin outer disk, which is too low to efficiently photoionize the K shell. For this reason, we conclude that the production of K and L seed photons in the outer burst is about equal, and therefore we set $N_{\rm L2} = N_{\rm K2}$.

Another important ingredient in the coupled-burst model developed here is the time delay between the first burst at radius r_1 and the second burst at radius r_2. The physical interpretation of this delay is the propagation time required for the pressure wave that is generated at radius r_1 by the thermal instability to travel outward to the second source at radius r_2, located close to the standing shock at the outer edge of the hot, wedge-shaped inner region of the accretion flow. The effect of this propagation delay on the time lags computed using the coupled-burst model enters the calculations through the factor $e^{i\tilde{\omega} q_*}$ in Equation (60), which represents the complex phase shift for each burst. Because the energy dependence of the Green's function Fourier transform, $F_{\rm G}$, is different at the two source radii r_1 and r_2, this implies the existence of an energy-dependent phase shift between the two Fourier transforms, $\tilde{\mathscr{F}}_1$ and $\tilde{\mathscr{F}}_2$, that are summed together in Equation (69) to obtain the total Fourier transformation used to compute the theoretical X-ray time lags δt. Hence, in our coupled-burst model, the propagation time between the first and second bursts has an effect on the time lags, and consequently this must be taken into account when computing the value of Δq, which is connected with the values of r_1, r_2, and $\mathscr{M}$ via Equation (72).

The theoretical framework developed here is based on the self-similar dynamical model for the accretion disk structure developed by R. D. Blandford & M. C. Begelman (1999). While these authors focused on the structure of ADAF disks, with sub-Eddington accretion rates, we argue that it is also likely to describe the structure of LHAF disks adequately well for our purposes here (F. Yuan 2001). LHAF disks are relevant in the case of the most luminous NLS1 sources, which are thought to contain black holes accreting with dimensionless rate $\dot{m} \sim 1$. It is apparent that the new coupled-burst model developed here is able to reproduce the complexity of the time lag distributions for each of the sources, including multiple changes of sign, indicating separate discrete transitions between hard-lag and soft-lag behaviors.

5.2. Relation to Variability of X-Ray Continuum

In this paper, we have studied the time-dependent X-ray emission produced as a result of the reprocessing of iron K and L seed photons via thermal and bulk Comptonization, spatial advection, and diffusion occurring in the hot inner region of the accretion disk around the central black hole. While it is clear from the results presented in Figure 3 that our model is able to reproduce the observed Fourier time lag behaviors for the four sources we have analyzed, it is also important to explore how the mechanism investigated here is related to the overall variability properties of the observed X-ray continuum spectrum. We discuss this question here.

The X-ray time lags and the related relative rms variability of the X-ray continuum spectrum for 1H 0707−495 have been analyzed by L. C. Gallo et al. (2004) and A. C. Fabian et al. (2004, 2012) using data from observations performed in 2000, 2008, and 2011. These authors used the computed X-ray time lags to constrain the parameters for their reflection model for the source. It is interesting that while the time lag plots are relatively consistent over the three observed epochs, the behavior of the rms variability was distinctly different in 2000, 2008, and 2011. While our model is different from their reflection scenario in several ways, it is nonetheless incumbent on us to show that our model is in agreement with the range of time-dependent data that they analyzed.

We have demonstrated in Figure 3 that our model agrees with the time lag data for 1H 0707−495. The remaining comparison concerns the energy-dependent, dimensionless rms variability spectrum, $F_{\rm var}(\epsilon)$, which is calculated using the formula

$$F_{\rm var}^2(\epsilon) = \frac{1}{t_{\rm obs,\,2} - t_{\rm obs,\,1}} \frac{1}{\langle \mathscr{F}_\epsilon(\epsilon)\rangle^2} \times \int_{t_{\rm obs,\,1}}^{t_{\rm obs,\,2}} (\mathscr{F}_\epsilon(t,\,\epsilon) - \langle \mathscr{F}_\epsilon(\epsilon)\rangle)^2\, dt, \tag{82}$$

or, equivalently,

$$F_{\rm var}^2(\epsilon) = \frac{1}{t_{\rm obs,\,2} - t_{\rm obs,\,1}} \frac{1}{\langle \mathscr{F}_\epsilon(\epsilon)\rangle^2} \int_{t_{\rm obs,\,1}}^{t_{\rm obs,\,2}} \mathscr{F}_\epsilon^2(t,\,\epsilon)\, dt - 1, \tag{83}$$

where $\mathscr{F}_\epsilon(t,\,\epsilon)$ is the observed flux spectrum, $t_{\rm obs,1}$ and $t_{\rm obs,2}$ denote the boundaries of the observational time window, and $\langle F_\epsilon(\epsilon)\rangle$ is the mean (time-averaged) spectrum, defined by

$$\langle \mathscr{F}_\epsilon(\epsilon)\rangle \equiv \frac{1}{t_{\rm obs,\,2} - t_{\rm obs,\,1}} \int_{t_{\rm obs,\,1}}^{t_{\rm obs,\,2}} \mathscr{F}_\epsilon(t,\,\epsilon)\, dt. \tag{84}$$

The function $\langle \mathscr{F}_\epsilon(\epsilon)\rangle$ represents the steady-state background spectrum, around which the random component of the signal fluctuates.

The theoretical framework we have developed here is derived in the Fourier domain, and therefore the evaluation of the variability spectrum $F_{\rm var}^2(\epsilon)$ is most straightforwardly accomplished by transforming the time integration in Equation (82) into a frequency integration. This can be achieved by using Parseval's theorem to write (J. D. Scargle 1989)

$$\int_{t_{\rm obs,\,1}}^{t_{\rm obs,\,2}} \mathscr{F}_\epsilon^2(t,\,\epsilon)\, dt = \frac{1}{2\pi} \int_{\omega_{\rm min}}^{\omega_{\rm max}} |\tilde{\mathscr{F}}_\epsilon(\omega,\,\epsilon)|^2\, d\omega, \tag{85}$$

where $\omega_{\rm min}$ and $\omega_{\rm max}$ denote the minimum and maximum Fourier frequencies based on the time range and temporal resolution of the data, and $\tilde{\mathscr{F}}_\epsilon(\omega,\,\epsilon)$ represents the Fourier transform of the observed spectrum at Fourier frequency ω and photon energy ϵ, which is related to the time-dependent spectrum, $\mathscr{F}_\epsilon(t,\,\epsilon)$, via

$$\tilde{\mathscr{F}}_\epsilon(\omega,\,\epsilon) \equiv \int_{t_{\rm obs,1}}^{t_{\rm obs,\,2}} \mathscr{F}_\epsilon(t,\,\epsilon)\, e^{i\omega t}\, dt. \tag{86}$$

In our application, $\tilde{\mathscr{F}}_\epsilon$ corresponds to the total transform for the coupled-burst model, $\tilde{\mathscr{F}}_{\rm total}$, which is computed using Equation (69).

We can combine Equations (83) and (85) to show that the dimensionless rms variability spectrum, $F_{\rm var}(\epsilon)$, can be computed using

$$F_{\rm var}^2(\epsilon) = \frac{1}{t_{\rm obs,\,2} - t_{\rm obs,\,1}} \frac{1}{\langle \mathscr{F}_\epsilon(\epsilon)\rangle^2} \times \frac{1}{2\pi} \int_{\omega_{\rm min}}^{\omega_{\rm max}} |\tilde{\mathscr{F}}_\epsilon(\omega,\,\epsilon)|^2\, d\omega - 1. \tag{87}$$

Our remaining task is to evaluate the time-averaged (steady-state) X-ray spectrum, $\langle \mathscr{F}_\epsilon(\epsilon)\rangle$, appearing in Equation (87). This function can be computed by evaluating the Fourier-transformed flux, $\tilde{\mathscr{F}}_\epsilon(\omega,\,\epsilon)$, at Fourier frequency $\omega = 0$. To see this, we define the Fourier transform of the steady-state spectrum using

$$\tilde{\mathscr{F}}_\epsilon^{\rm SS}(\omega,\,\epsilon) \equiv \int_{t_{\rm obs,\,1}}^{t_{\rm obs,\,2}} \langle \mathscr{F}_\epsilon(\epsilon)\rangle\, e^{i\omega t}\, dt. \tag{88}$$

Setting $\omega = 0$ then yields

$$\tilde{\mathscr{F}}_\epsilon^{\rm SS}(0,\,\epsilon) \equiv \int_{t_{\rm obs,1}}^{t_{\rm obs,\,2}} \langle \mathscr{F}_\epsilon(\epsilon)\rangle\, dt = (t_{\rm obs,\,2} - t_{\rm obs,\,1})\, \langle \mathscr{F}_\epsilon(\epsilon)\rangle, \tag{89}$$

from which it follows that the steady-state spectrum, $\langle \mathscr{F}_\epsilon(\epsilon)\rangle$, is related to the Fourier transform via

$$\langle \mathscr{F}_\epsilon(\epsilon)\rangle = \frac{1}{t_{\rm obs,\,2} - t_{\rm obs,\,1}} \tilde{\mathscr{F}}_\epsilon^{\rm SS}(0,\,\epsilon). \tag{90}$$

Next we recognize that the function $\tilde{\mathscr{F}}_\epsilon^{\rm SS}(\omega,\,\epsilon)$ is related to the transform of the time-dependent spectrum, $\tilde{\mathscr{F}}_\epsilon(\omega,\,\epsilon)$, via

$$\tilde{\mathscr{F}}_\epsilon^{\rm SS}(0,\,\epsilon) = \tilde{\mathscr{F}}_\epsilon(0,\,\epsilon), \tag{91}$$

which can be combined with Equation (90) to conclude that

$$\langle \mathscr{F}_\epsilon(\epsilon)\rangle = \frac{1}{t_{\rm obs,\,2} - t_{\rm obs,\,1}} \tilde{\mathscr{F}}_\epsilon(0,\,\epsilon). \tag{92}$$

We can now use Equation (92) to substitute for $\langle \mathscr{F}_\epsilon(\epsilon)\rangle$ in Equation (87) to obtain the final result

$$F_{\rm var}^2(\epsilon) = (t_{\rm obs,\,2} - t_{\rm obs,\,1}) \frac{1}{\tilde{\mathscr{F}}_\epsilon^2(0,\,\epsilon)} \frac{1}{2\pi} \times \int_{\omega_{\rm min}}^{\omega_{\rm max}} |\tilde{\mathscr{F}}_\epsilon(\omega,\,\epsilon)|^2\, d\omega - 1. \tag{93}$$

This expression can be used to quantify the variability of the X-ray emission in the context of our model if we replace the general transform $\tilde{\mathscr{F}}_\epsilon$ in Equation (93) with the total transform for the coupled-burst model, $\tilde{\mathscr{F}}_{\rm total}$, computed using Equation (69).

As an example application, we will use Equation (93) to study the variability of the X-ray continuum in 1H 0707−495 using our model. In Figure 4, we plot the relative variability spectrum, $F_{\rm var}(\epsilon)$, computed using Equation (93) with $\tilde{\mathscr{F}}_\epsilon = \tilde{\mathscr{F}}_{\rm total}$

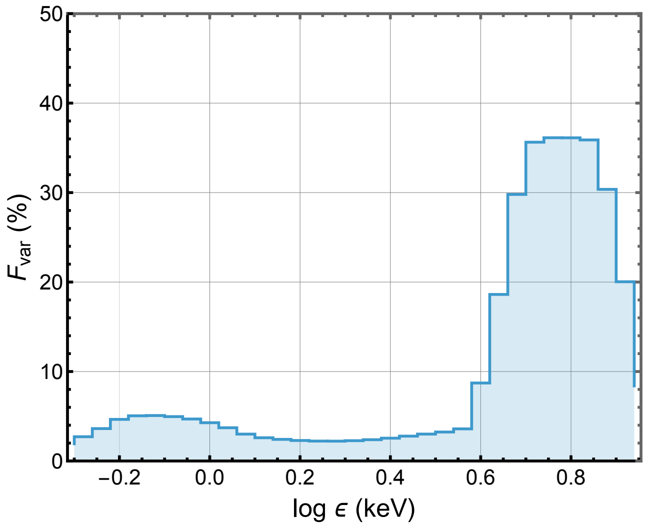

Figure 4. Relative rms variability of the time-dependent X-ray signal around the mean value, $F_{\rm var}$, plotted as a function of the photon energy, ϵ. This result is obtained using Equation (93) with the general transform, $\tilde{\mathscr{F}}_\epsilon$, replaced with the total transform for the coupled-burst model, $\tilde{\mathscr{F}}_{\rm total}$, computed using Equation (69). Note the prominence of the variability in the region of the iron K line, with energy $\epsilon \sim 6$ keV. Enhanced variability is also visible in the vicinity of the iron L line, with energy $\epsilon \sim 1$ keV. The behavior depicted here is qualitatively similar to Figure 9 from A. C. Fabian et al. (2004).

evaluated using Equation (69) as a function of the photon energy ϵ with $t_{\rm obs,2} - t_{\rm obs,1} = 10^5$ s. The theoretical result displays the prominent variability around photon energy $\epsilon \sim 6$ keV, corresponding to the iron K line. The region around the iron L line, with energy $\epsilon \sim 1$ keV, also exhibits enhanced variability relative to the mean spectrum. We note that the overall level of the X-ray emission varies by ∼20% relative to the mean spectrum in the vicinity of the K line, in accordance with the light curves for 1H 0707−495 analyzed by A. C. Fabian et al. (2004, 2012) and L. C. Gallo et al. (2004). In particular, the behavior plotted in Figure 4 is qualitatively similar to that depicted in Figure 9 in A. C. Fabian et al. (2004).

5.3. Comparison with Previous Work

In this paper, we have developed a new model for the time-dependent X-ray emission from NLS1 galaxies produced as a consequence of the reprocessing of fluorescent iron L and K photons that are generated in two coupled bursts occurring in the inner hot region of the accretion disk. The bursts are powered by transient X-ray emission from the hot central corona, with a power-law photon number spectrum given by Equation (1). The X-ray emission from the corona is produced by energetic electrons accelerated by impulsive magnetic reconnection events (J. Malzac & E. Jourdain 2000; A. Zoghbi et al. 2010; D. R. Wilkins et al. 2022). A large fraction of the X-ray emission from the corona may be gravitationally deflected downward to illuminate the underlying disk, generating iron fluorescence. However, a significant portion of the emission from the corona may be directly observable (L. Miller et al. 2010a, 2010b). The X-rays that illuminate the disk may also undergo thermal reprocessing before escaping to contribute to the observed X-ray continuum in NLS1 sources (A. Zoghbi et al. 2010; A. C. Fabian et al. 2012).

The production of fluorescent iron K and L photons in our model and their subsequent reprocessing via Compton scattering and advection, also called Compton reverberation, is a variation of the standard reflection scenario that focuses on detailed analysis of the time-dependent radiative transfer occurring in the region of the disk illuminated by the hot corona (A. C. Fabian et al. 2004, 2012). The reprocessing of iron L photons, with injection energy $\epsilon \sim 0.7$ keV, via bulk and thermal Comptonization tends to create hard lags because the injection energy is below the thermal energy of the electrons, $k_{\rm B}T_e \sim 10-20$ keV (see Table 1). On the other hand, the reprocessing of K photons, with injection energy $\epsilon \sim 6.4$ keV, tends to occur via downscattering, which induces soft lags. The interplay between these two mechanisms can produce multiple sign changes in the time lag distribution, as observed in the four NLS1 sources treated here, and in a number of others as well (e.g., B. De Marco et al. 2013). The incorporation of these effects in our model leads to enhanced agreement between the theoretical predictions and the observational time lag data, as is evident from the reduced chi-square values (as compared with the single-burst model), making it more comprehensive and accurate than any of the previous models for time lags, which tend to be ad hoc and composed of a number of disparate physical mechanisms, as discussed in Section 1.2.

We find that the existence of two coupled bursts of iron K and L photons is required in order to explain the complexity of the dependence of X-ray time lags on the Fourier frequency for sources that display multiple transitions between hard lags and soft lags, such as NGC 4051 and Mrk 766, with each transition indicated by a change in sign of the time lag δt. This behavior was recognized in a qualitative sense by D. C. Baughman & P. A. Becker (2022) and Paper I, which suggested that the time lag changes sign at the critical Fourier frequency, $\nu_{\rm F}^{\rm crit}$, because the iron L photon energy, $\epsilon_{\rm L} \sim 0.89$ keV, falls between the soft and hard detector band energies that are used to compute the time lags. By inspection of the time lag results plotted in Figure 3 for the four NLS1 galaxies treated here, we see that the Fourier frequency $\nu_{\rm F}^{\rm crit}$ where the time lag changes sign is in the range $10^{-3.5}$ Hz $\leqslant \nu_{\rm F}^{\rm crit} \leqslant 10^{-3.2}$ Hz, agreeing with the discussion in Paper I and the work of D. C. Baughman & P. A. Becker (2022). The hard lags occurring on long timescales, or equivalently at small Fourier frequencies $\nu_{\rm F}$, result from electron recoil losses, which happen faster than the stochastic energization. This effect delays the production of high-energy photons relative to low-energy photons. On the other hand, the soft lags at high $\nu_{\rm F}$ are due to rapid photon energization in a single collision, which overwhelms recoil losses on short timescales (T. R. Lewis et al. 2016).

It is important to note that although we have focused on the reprocessing of K and L seed photons resulting from a single flash of X-rays from the central corona, in reality we anticipate a random series of instabilities occurring over time. It can be shown that the Fourier transforms of the radiation distributions resulting from each of these random transients are all identical to each other (D. C. Baughman & P. A. Becker 2022). Therefore, due to the linear nature of the fundamental transport equation (Equation (33)), the total Fourier transform obtained by summing over the random series of instabilities will have the same complex structure as the fundamental Green's function solution obtained here, given by Equation (60). Hence, it follows that our solution for the Fourier transform of the observed radiation field given by Equation (69) correctly describes the total variability, and therefore our result for the theoretical X-ray time lag, δt, remains valid.

5.4. Conclusion

Based on the results presented in Section 4 and plotted in Figure 3, we conclude that our coupled-burst Compton reverberation model represents the first comprehensive theoretical framework that is able to adequately fit the time lag data for a wide variety of NLS1 sources, including those for which the sign of the time lag changes multiple times as a function of the Fourier frequency. This is indicated by the lower reduced chi-square value, $\chi^2_{\rm CB}$, obtained using the coupled-burst model, as compared with the value of $\chi^2_{\rm SB}$ obtained using the single-burst model developed in Paper I. We therefore argue that our coupled-burst model provides the most self-consistent explanation for the production of Fourier time lags in the X-ray emission from black hole accretion disks.

The new coupled-burst model developed here proves remarkably successful at qualitatively fitting the time lag data for multiple NLS1 sources, but nonetheless it is important to discuss the limitations of the model and the associated implications for future work. The model does not include a detailed calculation of the ionization structure of the plasma in the accretion disk, which is beyond the scope of this paper. However, we intend to include this physical effect in a future version of the model in order to more rigorously treat the thermal structure of the accretion disk. The coupled-burst model includes the time-dependent X-ray emission escaping from both the face and the edge of the accretion disk, and consequently there is a strong dependence on the inclination angle θ, which can be used to test the model by comparing the value of θ we obtain with the value obtained using independent methods for a broader group of NLS1 galaxies.

Acknowledgments

We would like to thank the Office of Research Computing at George Mason University (URL: https://orc.gmu.edu) for the partial support of computing resources and the Office of the Provost and the Department of Physics and Astronomy at George Mason University for the funding. We are also grateful to the anonymous referee who provided several useful comments that led to significant improvements in the manuscript.

Software: Wolfram Mathematica 14.0 and 14.2.

Author Contribution

All authors contributed equally to the Terra Mater collaboration.

ORCID iDs

Thunyapong Mahapol https://orcid.org/0009-0009-2527-0393
Peter A. Becker https://orcid.org/0000-0002-3718-1293
Mario Gliozzi https://orcid.org/0000-0002-8818-9009

References

Abramowitz, M., Stegun, I. A., & Romer, R. H. 1988, AmJPh, 56, 958
Alston, W., Boorman, P., Bulgarelli, A., & Parker, M. 2020, in Tutorial Guide to X-Ray and Gamma-Ray Astronomy: Data Reduction and Analysis, ed. C. Bambi (Springer), 229
Arévalo, P., & Uttley, P. 2006, MNRAS, 367, 801
Bardeen, J. M., Press, W. H., & Teukolsky, S. A. 1972, ApJ, 178, 347
Barua, S., Jithesh, V., Misra, R., et al. 2020, MNRAS, 492, 3041
Baughman, D. C., & Becker, P. A. 2022, ApJ, 932, 113
Becker, P. A. 2003, MNRAS, 343, 215
Bentz, M. C., & Katz, S. 2015, PASP, 127, 67
Bentz, M. C., Walsh, J. L., Barth, A. J., et al. 2009, ApJ, 705, 199
Blandford, R. D., & Begelman, M. C. 1999, MNRAS, 303, L1
Boller, T., Brandt, W. N., & Fink, H. 1996, A&A, 305, 53
Boller, T., Liu, T., Weber, P., et al. 2021, A&A, 647, A6
Buisson, D. J. K., Parker, M. L., Kara, E., et al. 2018, MNRAS, 480, 3689
Chakrabarti, S., & Titarchuk, L. G. 1995, ApJ, 455, 623
Chakrabarti, S. K. 1997a, ASPC, 121, 427
Chakrabarti, S. K. 1997b, ApJ, 484, 313
Colpi, M. 1988, ApJ, 326, 223
Dauser, T., Svoboda, J., Schartel, N., et al. 2012, MNRAS, 422, 1914
De Marco, B., Ponti, G., Cappi, M., et al. 2013, MNRAS, 431, 2441
Denney, K. D., Watson, L. C., Peterson, B. M., et al. 2009, ApJ, 702, 1353
Done, C., & Jin, C. 2016, MNRAS, 460, 1716
Duras, F., Bongiorno, A., Ricci, F., et al. 2020, A&A, 636, A73
Fabian, A. C., Ballantyne, D. R., Merloni, A., et al. 2002, MNRAS, 331, L35
Fabian, A. C., Miniutti, G., Gallo, L., et al. 2004, MNRAS, 353, 1071
Fabian, A. C., & Vaughan, S. 2003, MNRAS, 340, L28
Fabian, A. C., Zoghbi, A., Ross, R. R., et al. 2009, Natur, 459, 540
Fabian, A. C., Zoghbi, A., Wilkins, D., et al. 2012, MNRAS, 419, 116
Fukumura, K., Hendry, D., Clark, P., Tombesi, F., & Takahashi, M. 2016, ApJ, 827, 31
Gallo, L. C. 2006, MNRAS, 368, 479
Gallo, L. C., Tanaka, Y., Boller, T., et al. 2004, MNRAS, 353, 1064
Gardner, E., & Done, C. 2014, MNRAS, 442, 2456
Giacchè, S., Gilli, R., & Titarchuk, L. 2014, A&A, 562, A44
Guainazzi, M., Nicastro, F., Fiore, F., et al. 1998, MNRAS, 301, L1
Haardt, F., & Maraschi, L. 1991, ApJL, 380, L51
Haardt, F., & Maraschi, L. 1993, ApJ, 413, 507
Hameury, J., Viallet, M., & Lasota, J. 2009, A&A, 496, 413
Hasinger, G., Langmeier, A., Sztajno, M., et al. 1986, Natur, 319, 469
Hua, X.-M., Kazanas, D., & Cui, W. 1999, ApJ, 512, 793
Hua, X.-M., Kazanas, D., & Titarchuk, L. 1997, ApJL, 482, L57
Kaastra, J. S., & Mewe, R. 1993, A&AS, 97, 443
Kara, E., Fabian, A. C., Cackett, E. M., et al. 2013a, MNRAS, 428, 2795
Kara, E., Fabian, A. C., Cackett, E. M., et al. 2013b, MNRAS, 434, 1129
Kara, E., García, J. A., Lohfink, A., et al. 2017, MNRAS, 468, 3489
Komossa, S. 2008, RMxAC, 32, 86
Koss, M. J., Ricci, C., Trakhtenbrot, B., et al. 2022, ApJS, 261, 2
Krause, M. O. 1979, JPCRD, 8, 307
Kroon, J. J., & Becker, P. A. 2016, ApJ, 821, 77
Lawther, D., Vestergaard, M., Raimundo, S., et al. 2023, MNRAS, 519, 3903
Le, T., & Becker, P. A. 2005, ApJ, 632, 476
Lewis, T. R., Becker, P. A., & Finke, J. D. 2016, ApJ, 824, 108
Lyubarskii, Y. E. 1997, MNRAS, 292, 679
Mahapol, T., & Becker, P. A. 2024, MNRAS, 529, 4156
Malzac, J., & Jourdain, E. 2000, A&A, 359, 843
Marshall, F. E., Holt, S. S., Mushotzky, R. F., & Becker, R. H. 1983, ApJL, 269, L31
Martocchia, A., & Matt, G. 1996, MNRAS, 282, L53
Meena, B., Crenshaw, D. M., Schmitt, H. R., et al. 2021, ApJ, 916, 31
Miller, L., Turner, T. J., Reeves, J. N., & Braito, V. 2010a, MNRAS, 408, 1928
Miller, L., Turner, T. J., Reeves, J. N., et al. 2010b, MNRAS, 403, 196
Miniutti, G., & Fabian, A. C. 2004, MNRAS, 349, 1435
Miyamoto, S., Kitamoto, S., Mitsuda, K., & Dotani, T. 1988, Natur, 336, 450
Mizumoto, M., Ebisawa, K., Tsujimoto, M., et al. 2018, MNRAS, 482, 5316
Mizumoto, M., Ebisawa, K., Tsujimoto, M., et al. 2019, MNRAS, 482, 5316
Narayan, R., & Yi, I. 1995, ApJ, 444, 231
Nowak, M. A., Vaughan, B. A., Wilms, J., Dove, J. B., & Begelman, M. C. 1999, ApJ, 510, 874
Oh, K., Ueda, Y., Yamada, S., et al. 2025, PASJ, 77, 562
Papadakis, I. E., Brinkmann, W., Page, M. J., Mc Hardy, I., & Uttley, P. 2007, A&A, 461, 931
Peterson, B. M., Ferrarese, L., Gilbert, K. M., et al. 2004, ApJ, 613, 682
Pounds, K. A., Reeves, J. N., King, A. R., & Page, K. L. 2004, MNRAS, 350, 10
Rybicki, G. B., & Lightman, A. P. 1979, Radiative Processes in Astrophysics (Wiley)
Scargle, J. D. 1989, ApJ, 343, 874

Seifina, E., Chekhtman, A., & Titarchuk, L. 2018, A&A, 613, A48
Singh, V., Shastri, P., & Risaliti, G. 2011, A&A, 533, A128
Sunyaev, R. A., & Titarchuk, L. G. 1980, A&A, 86, 121
Szanecki, M., Niedźwiecki, A., Done, C., et al. 2020, A&A, 641, A89
Terashima, Y., Gallo, L. C., Inoue, H., et al. 2009, PASJ, 61, S299
Titarchuk, L., & Seifina, E. 2017, A&A, 602, A113
Uttley, P., Cackett, E. M., Fabian, A. C., Kara, E., & Wilkins, D. R. 2014, A&ARv, 22, 72
van der Klis, M., Hasinger, G., Stella, L., et al. 1987, ApJL, 319, L13
Vasudevan, R. V., & Fabian, A. C. 2007, MNRAS, 381, 1235
Vasudevan, R. V., Fabian, A. C., Gandhi, P., Winter, L. M., & Mushotzky, R. F. 2010, MNRAS, 402, 1081
Wilkins, D. R., Cackett, E. M., Fabian, A. C., & Reynolds, C. S. 2016, MNRAS, 458, 200
Wilkins, D. R., Gallo, L. C., Costantini, E., Brandt, W. N., & Blandford, R. D. 2022, MNRAS, 512, 761
Xu, Y., Pinto, C., Bianchi, S., et al. 2021, MNRAS, 508, 6049
Yuan, F. 1999, ApJL, 521, L55
Yuan, F. 2001, MNRAS, 324, 119
Zoghbi, A., Fabian, A. C., Uttley, P., et al. 2010, MNRAS, 401, 2419